

Quantifying the chemical desorption of H₂S and PH₃ from amorphous water ice surfaces

KENJI FURUYA,¹ YASUHIRO OBA,² AND TAKASHI SHIMONISHI^{3,4}

¹*National Astronomical Observatory of Japan, Osawa 2-21-1, Mitaka, Tokyo 181-8588, Japan*

²*Institute of Low Temperature Science, Hokkaido University, Sapporo, Hokkaido 060-0819, Japan*

³*Center for Transdisciplinary Research, Niigata University, Ikarashi-nincho 8050, Nishi-ku, Niigata, 950-2181, Japan*

⁴*Environmental Science Program, Department of Science, Faculty of Science, Niigata University, Ikarashi-nincho 8050, Nishi-ku, Niigata, 950-2181, Japan*

(Received; Revised; Accepted)

Submitted to ApJ

ABSTRACT

Nonthermal desorption of molecules from icy grain surfaces is required to explain molecular line observations in the cold gas of star-forming regions. Chemical desorption is one of the nonthermal desorption processes and is driven by the energy released by chemical reactions. After an exothermic surface reaction, the excess energy is transferred to products' translational energy in the direction perpendicular to the surface, leading to desorption. The desorption probability of product species, especially that of product species from water ice surfaces, is not well understood. This uncertainty limits our understanding of the interplay between gas-phase and ice surface chemistry. In the present work, we constrain the desorption probability of H₂S and PH₃ per reaction event on porous amorphous solid water (ASW) by numerically simulating previous laboratory experiments. Adopting the microscopic kinetic Monte Carlo method, we find that the desorption probabilities of H₂S and PH₃ from porous ASW per hydrogen addition event of the precursor species are $3 \pm 1.5\%$ and $4 \pm 2\%$, respectively. These probabilities are consistent with a theoretical model of chemical desorption proposed in the literature if $\sim 7\%$ of energy released by the reactions is transferred to the translational excitation of the products. As a byproduct, we find that approximately 70% (40%) of adsorption sites for atomic H on porous ASW should have a binding energy lower than ~ 300 K (~ 200 K). The astrochemical implications of our findings are briefly discussed.

Keywords: Astrochemistry(75) — Reaction catalysts(2080) — Interstellar molecules(849) — Interstellar dust processes(838)

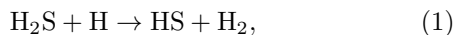
1. INTRODUCTION

Various molecules have been detected in the cold (~ 10 K) gas of star-forming regions (see e.g., McGuire 2018). Some molecules, such as CO and N₂H⁺, have gas-phase production pathways that are sufficiently efficient to explain their observed abundances, whereas others, such as CH₃OH and H₂S, do not form by gas-phase reactions efficiently enough to explain the observations (e.g., Geppert et al. 2006; Garrod et al. 2007). Molecules of the latter type are thought to form on dust grains

via surface reactions, and to be released into the gas phase via nonthermal desorption processes because thermal desorption is negligible at 10 K. Thus far, several mechanisms of nonthermal desorption have been proposed, including UV photodesorption (e.g., Hama et al. 2009; Bertin et al. 2016; Fuente et al. 2017), stochastic heating and/or sputtering by cosmic rays (e.g., Dartois et al. 2015; Ivlev et al. 2015), and chemical desorption (e.g., Dulieu et al. 2013; Minissale et al. 2016; He et al. 2017; Chuang et al. 2018; Oba et al. 2018; Nguyen et al. 2020). A quantitative understanding of nonthermal desorption processes is critical for understanding the interplay between gas-phase and ice surface chemistry.

Among nonthermal desorption processes, chemical desorption is the topic of the present paper. Chemical desorption is caused by the energy released by chemical reactions; after an exothermic surface reaction, (the part of) excess energy goes into the products' translational energy in the direction perpendicular to the surface, leading to desorption (e.g., Fredon et al. 2017). Laboratory experiments have demonstrated that chemical desorption indeed occurs in several reaction systems on astrophysically relevant surfaces (e.g., Dulieu et al. 2013; Minissale et al. 2016; He et al. 2017; Chuang et al. 2018; Oba et al. 2018). In most of these studies, chemical desorption was quantified solely by gas-phase measurements using quadrupole mass spectroscopy (QMS) even though chemical desorption is a surface process. One important result obtained from these experiments is that the fraction of reaction products desorbed from the surface depends on both the reaction and the surface composition. The fraction on amorphous solid water (ASW) is lower than that on graphite or silicate surfaces (Minissale et al. 2016). For some of the reactions studied thus far (e.g., $O + O \rightarrow O_2$), the fraction of reaction products released from the surface is reported to be several tens of percent on graphite/silicate surfaces; by contrast, on ASW, it falls below the upper limit of $\sim 10\%$ measurable in the experiments (see Table 1 in Minissale et al. 2016, for summary). Quantitative understanding of the chemical desorption process, in particular, on ASW is limited because of its low efficiency, although ASW would be more representative of the surface of interstellar grains in star-forming regions than graphite/silicate. Because of our limited understanding of chemical desorption, current astrochemical models often assume that the desorption probability per reactive event is $\sim 1\%$ (e.g., Garrod 2013; Taquet et al. 2014; Furuya et al. 2015).

For better understanding of chemical desorption on ASW, researchers have conducted experimental studies in which time-resolved infrared measurements were used to monitor surface species (Oba et al. 2018, 2019; Nguyen et al. 2020, 2021, see also Chuang et al. (2018) for chemical desorption due to reactions involving CO and hydrogen). Oba et al. (2018, 2019) studied chemical desorption upon the reaction of H_2S with H atoms on ASW. They deposited atomic H onto ASW partly covered by H_2S . The following reactions can occur in this system:



Reactions 1 and 2 are exothermic, with exothermicities of 58 kJ mol^{-1} (corresponding to $\sim 7000 \text{ K}$) and 374

kJ mol^{-1} ($\sim 45,000 \text{ K}$), respectively (Oba et al. 2018), which are much larger than the binding energies of H_2S and HS on ASW (2700 K ; Collings et al. 2004; Wakelam et al. 2017). HS is formed from H_2S via a hydrogen abstraction reaction, and hydrogenation of HS leads to the (re)formation of H_2S . H_2S and HS can desorb by chemical desorption in each cycle of this H_2S –HS loop. Because the H_2S –HS loop can continue as long as H atoms are available, a substantial fraction of H_2S and HS can desorb from the ASW surface during H-atom deposition, even if the probability of chemical desorption per reactive event is small. In Oba et al. (2019), during atomic H deposition experiments, the authors monitored the abundance of H_2S on ASW by Fourier transform infrared (FTIR) spectroscopy. During H-atom deposition, a decrease in the intensity of the band at 2570 cm^{-1} , which was assigned to the S–H stretching band of H_2S , was observed. Reaction 1 has an activation energy barrier of 1560 K (Lamberts & Kästner 2017), whereas Reaction 2 is barrierless. Most S on ASW might exist as H_2S during the H_2S –HS loop (this is discussed in Section 3). If so, the decrease in the intensity of the band at 2570 cm^{-1} should be due to chemical desorption of H_2S and/or HS. They found that the amount of H_2S on porous ASW gradually decreased with time (i.e., with increasing amount of H-atom deposition), that $\sim 60\%$ of the initial amount of H_2S was eventually lost from the ASW surface in experiments at 10 K and 20 K , and that $\sim 30\%$ was lost in an experiment at 30 K . Although the dominant chemical form of S released from the surface (either H_2S or HS) could not be identified, H_2S could be the dominant form because the exothermicity of Reaction 2 is greater than that of Reaction 1 (Oba et al. 2018).

Nguyen et al. (2020, 2021) experimentally studied the chemical desorption process upon reaction of PH_3 with H atoms on ASW in experiments similar to those of Oba et al. (2018, 2019). They deposited atomic H onto ASW, which was partly covered by PH_3 . The following reactions can occur in this system:



Reactions 3 and 4 are exothermic, with exothermicities of 81.5 kJ mol^{-1} and $337.5 \text{ kJ mol}^{-1}$, respectively (Molpeceres & Kästner 2021). Similar to the H_2S –HS loop, interconversion between PH_3 and PH_2 occurs through Reactions 3 and 4. In their experiments at 10 K , $\sim 80\%$ of the initial amount of PH_3 deposited onto porous ASW was released from the surface.

Oba et al. (2019) and Nguyen et al. (2021) estimated a chemical desorption probability *per reactive species*

(i.e., per incident H atoms) of $\sim 1\%$ on porous ASW for the H₂S + H and PH₃ + H systems. As noted by Oba et al. (2018), the desorption probability per incident H atom corresponds to the lower limit of the desorption probability *per reactive event*, which astrochemical models require as inputs. This is because H atoms adsorbed onto ASW surfaces can be thermally desorbed or consumed by the H₂ formation via the recombination of two H atoms on the surface. The primary goal of this paper is to constrain the desorption probability of H₂S and PH₃ per reaction event on porous ASW on the basis of the experimental data reported by Oba et al. (2019) and Nguyen et al. (2021), respectively. To this end, we conduct kinetic Monte Carlo simulations of their experiments.

The rest of this paper is organized as follows: our numerical model is described in Section 2, and the results are described in Section 3. We compare our derived desorption probability with the theoretical predictions reported in the literature in Section 4. The astrochemical implications of the chemical desorption of H₂S and PH₃ are briefly discussed. We summarize our findings in Section 5.

2. METHODS

We intend to constrain the chemical desorption probability per reaction event (P_{cd}) for H₂S + H and PH₃ + H systems on porous ASW by numerically simulating the experiments of Oba et al. (2019) and Nguyen et al. (2021). For this purpose, we adopt an on-lattice kinetic Monte Carlo (kMC) method (Gillespie 1976; Cuppen et al. 2013). In our kMC model, a sequence of processes—adsorption, thermal hopping, and desorption—are modeled as a Markov chain adopting the next reaction method (e.g., Gibson & Bruck 2000; Chang & Herbst 2012). In the case of thermal hopping, a hop in a different direction is treated as a distinct event. This sequence is chosen on the basis of random numbers in combination with the rates for these processes. In contrast to the rate-equation method, which is widely used in the astrochemical community, the position and movement of each chemical species on surfaces are tracked over time in our kMC simulations. Consideration of the binding energy distribution on surfaces in the kMC simulations is then straightforward. Water ice surfaces are known to contain various adsorption sites with different energy depths (e.g., Amiaud et al. 2006; Hama et al. 2012; Karssemeijer et al. 2014). We will show that the binding energy distribution of atomic H is a key parameter for reproducing the experiments (see Section 3). Details of the numerical aspects of the

kMC method can be found in Chang & Herbst (2012), Cuppen et al. (2013), and references therein.

Oba et al. (2019) experimentally investigated the surface reactions of H₂S with H atoms on porous ASW, nonporous ASW, and polycrystalline water ice. They found no strong correlation between the ice structure and the desorption probability per incident H atom in their experiments at 10 K. In the present work, we focus on experiments on porous ASW because the experiments were conducted at three different surface temperatures: 10 K, 20 K, and 30 K. For nonporous ASW and polycrystalline water ice, the experiments were conducted only at 10 K. As shown later, we need experimental data at different surface temperatures to constrain the P_{cd} and resolve the degeneracy between parameters—in particular, the binding energy distribution for atomic H and the P_{cd} . Notably, the P_{cd} is assumed to be independent of the surface temperature throughout this work. This assumption would be reasonable because the exothermicity of Reactions 1–4 is much greater than the surface temperature.

For the surface reactions of PH₃ with H atoms, the experiments were conducted on porous ASW only at 10 K (Nguyen et al. 2021). Nonetheless, the P_{cd} for the PH₃ + H system can be constrained because we can constrain the binding energy distribution of atomic H by modeling the H₂S + H system. Similar to the H₂S + H system, that the desorption probability for PH₃ per incident H atom does not depend on the ice structure (Nguyen et al. 2021).

2.1. Numerical setup

A square grid is considered with an $n \times n$ square lattice providing, at each point, an adsorption site for chemical species on porous ASW. Each site thus has four neighboring sites. Periodic boundary conditions are used. Six different chemical species—atomic H, H₂, H₂S, HS, PH₃, and PH₂—are considered in our models. These different chemical species are assumed to share adsorption sites, whereas the binding energy of each species is assumed to differ even at the same site. Initially, some of the adsorption sites are occupied by H₂S or PH₃, as in the experiments by Oba et al. (2019) and Nguyen et al. (2021). The fluxes of H atoms onto the ASW surface are $5.7 \times 10^{13} \text{ cm}^{-2} \text{ s}^{-1}$ and $2.2 \times 10^{14} \text{ cm}^{-2} \text{ s}^{-1}$ for simulations of the H₂S + H experiments and the PH₃ + H experiments, respectively. These fluxes are consistent with those used in Oba et al. (2019) and Nguyen et al. (2021). We set the flux of H₂ to be two-thirds of that of H atoms because the H atoms are produced from H₂ with a dissociation probability of $>60\%$ (Oba et al.

2018). Refer to Section 2.2.1 for the sticking coefficients adopted in our models.

We consider thermal hopping and thermal desorption of H atoms and H₂ on the ASW surface, whereas those of H₂S, HS, PH₃, and PH₂ are ignored because their binding energies are relatively high ($\gtrsim 2000$ K, see Section 2.2.2 for details). If an H atom is adsorbed onto or hops to a site already occupied by another adsorbate, the two can react. For surface reactions, H₂ formation via recombination of two H atoms and Reactions 1–4 are considered. Table 1 summarizes the exothermicity, the activation energy barrier (if one exists), and the rate coefficient (s⁻¹) for Reactions 1–4. If a H₂ molecule is adsorbed onto or hops to a site already occupied by S-bearing or P-bearing species, the two do not react and we assume that H₂ is on the topmost layer at the site, with the adsorbate underneath. In this case, we assume that the binding energy of the H₂ is the same as that on porous ASW. We do not allow the adsorbate underneath a H₂ molecule to experience any chemical processes until the H₂ molecule desorbs or hops to a neighboring site. The presence of H₂ on the surface thus reduces the efficiency of surface reactions in our models. The slowing of surface reactions due to the presence of H₂ in laboratory experiments has been reported by Hama et al. (2015), who studied addition reactions of H atoms with solid benzene. Multiple layers of solid H₂ cannot be created even at 10 K (e.g., Hama et al. 2012). Then we assume that neither H₂ nor H atoms can be adsorbed onto or hop to a site already occupied by either H₂ or atomic H in our simulations. The exception is the adsorption of atomic H onto a site occupied by another atomic H, which instantly leads to the formation of H₂.

The thermal desorption rate (s⁻¹) of species i depends on its binding energy on the surface ($E_b(i)$),

$$k_{\text{des}}(i) = \nu_{\text{des}} \exp(-E_b(i)/kT_s), \quad (5)$$

where ν_{des} is the characteristic attempt frequency for thermal desorption (1.8×10^{12} s⁻¹; Amiaud et al. 2015), T_s is the surface temperature, and k is the Boltzmann constant. The binding energies adopted in our models are described in Section 2.2.2. Similarly, the surface diffusion rate for species i via thermal hopping depends on the hopping activation energy (E_{hop}):

$$k_{\text{diff, hop}}(i) = \nu_{\text{hop}} \exp(-E_{\text{hop}}/kT_s), \quad (6)$$

where ν_{hop} is the attempt frequency for hopping in one direction, and we arbitrarily assume that $\nu_{\text{des}} = \nu_{\text{hop}}$. The activation energy for hopping from a site with a binding energy of E_b to another site with a binding energy of E_b' is given as (Cazaux et al. 2017, see Fig. 1):

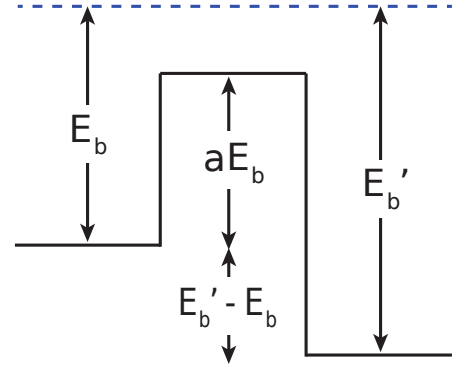


Figure 1. Schematic of the hopping activation barrier from one site to another when the two sites have different binding energies. Based on Fig. 11 in Cazaux et al. (2017).

$$E_{\text{hop}}(E_b \rightarrow E_b') = \alpha \times \min(E_b, E_b') + \max(0, E_b - E_b'), \quad (7)$$

where α , which is the hopping-to-binding energy ratio, is set to 0.65 for both atomic H and H₂, referring to the recommendation based on calculations of the diffusivity of atomic H on ASW (Asgeirsson et al. 2017). Given the expression for E_{hop} , the thermal hopping rate exhibits microscopic reversibility, i.e., $k_{\text{diff, hop}}(E_b \rightarrow E_b')/k_{\text{diff, hop}}(E_b' \rightarrow E_b) = \exp[-(E_b - E_b')/kT_s]$ (Cuppen et al. 2013). Although Eq. 6 is often used in kMC simulations (e.g., Cuppen & Herbst 2007; Garrod 2013), a different expression is proposed for the rate of hopping between adsorption sites with different potential-energy depths (Maté et al. 2020). We tested some models adopting Eq. 14 in Maté et al. (2020) instead of Eq. 6 and confirmed that the simulation results are not sensitive to the expression of the hopping rate. In our fiducial models, we do not consider the surface diffusion of atomic H by quantum tunneling. This effect will be discussed in Section 4.2.

For surface reactions, both the Langmuir–Hinshelwood mechanism and the Eley–Rideal mechanism are considered. In our model, when two species arrive at the same adsorption site and can undergo a chemical reaction, we do not follow the details of the competition but determine immediately which process—reaction, hopping, or desorption—occurs by comparing their rates (e.g., Cuppen & Herbst 2007; Chang & Herbst 2012). For barrierless reactions, we assume that the reaction occurs before desorption and hopping, with a probability of unity. For reactions with an activation barrier, the probability of the reaction occurring before one of the species (here, atomic H) leaves to the site, where the two species meet, is given by

$$p_{\text{A+H}} = \frac{k_{\text{A+H}}}{k_{\text{A+H}} + k_{\text{des}}(\text{H}) + \sum_{i=1}^4 k_{\text{diff, hop}}^i(\text{H})}, \quad (8)$$

Table 1. Summary of reaction properties

	(1) H ₂ S + H → HS + H ₂	(2) HS + H → H ₂ S	(3) PH ₃ + H → PH ₂ + H ₂	(4) PH ₂ + H → PH ₃
Reaction energy (kJ mol ⁻¹)	-58 ^a	-374 ^a	-81.5 ^c	-337.5 ^c
Activation energy (K)	1560 ^b	barrierless	1280 ^c	barrierless
Rate coefficient (s ⁻¹)	8.2 × 10 ⁶ d	-	8.7 × 10 ⁷ e	-

NOTE—^a Gas-phase values (Oba et al. 2018).

^b Lamberts & Kästner (2017).

^c Calculated values using a 20 water cluster model (Molpeceres & Kästner 2021).

^d Value at 55 K, which is the lowest temperature studied in quantum chemistry calculations by Lamberts & Kästner (2017). Note that quantum tunneling becomes important at $\lesssim 300$ K and that the rate constants at 70 K and 55 K are almost identical (Lamberts & Kästner 2017).

^e Value at 50 K, which is the lowest temperature studied in quantum chemistry calculations by Molpeceres & Kästner (2021).

where A is either H₂S or PH₃ and k_{A+H} is the reaction rate coefficient. The term $\sum_{i=1}^4 k_{\text{diff,hop}}^i$ originates from our assumption of a square lattice arrangement of surface sites; each site has four neighboring sites to which atomic H in the site can hop. Eq. 8 is implemented in the Monte Carlo algorithm as follows (Chang et al. 2007): A random number between 0 and 1 is generated. If this number is smaller than p_{A+H} , the reaction occurs. Otherwise, thermal desorption or hopping of the atomic H occurs on the basis of their rates and the random number.

Figure 2 shows $p_{\text{H}_2\text{S}+\text{H}}$ as functions of E_{hop} for atomic H at 10 K, 20 K, and 30 K under the assumption that E_{hop} is the same for hopping to the four neighboring sites. The value for parameter $k_{\text{H}_2\text{S}+\text{H}}$ was taken from Lamberts & Kästner (2017), who studied Reaction 1 using quantum chemical calculations (Table 1). At 10 K, $p_{\text{H}_2\text{S}+\text{H}}$ is unity (i.e., the reaction is effectively barrierless) when $E_{\text{hop}}(\text{H}) \gtrsim 150$ K. This threshold E_{hop} is higher for higher T_s because $k_{\text{diff,hop}}$ for a given E_{hop} increases with increasing T_s : it is 300 K and 450 K at $T_s = 20$ K and 30 K, respectively. Notably, as a result of the loop of H₂S–HS interconversion via Reactions 1 and 2, the HS/H₂S abundance ratio approaches $p_{\text{H}_2\text{S}+\text{H}}$.

After the surface reactions, the products are released from the surface via chemical desorption with a probability of P_{cd} (see Section 2.2.3). A random number between 0 and 1 is generated; if this number is smaller than the P_{cd} , the products are instantly released from the surface. Throughout this paper, we use the term “chemical desorption rate” as the rate of a surface reaction multiplied by the P_{cd} .

2.2. Chemical parameters

2.2.1. Sticking coefficient

The sticking coefficient depends on various parameters, such as the incident kinetic energy of colliding

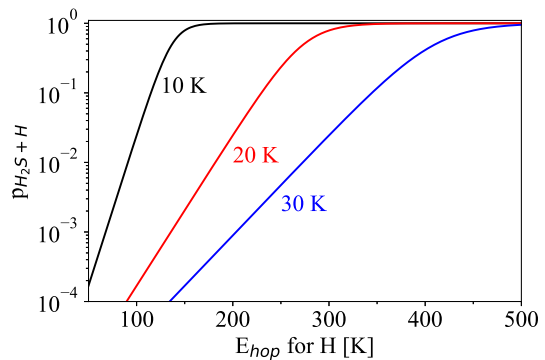


Figure 2. Probability for reactions to occur before thermal hopping of atomic H to a neighboring adsorption site occurs (Eq. 8), expressed as a function of the hopping activation energy at a surface temperature of 10 K (black), 20 K (red), and 30 K (blue). In this figure, E_{hop} is assumed to be the same for the four neighboring sites. Thermal desorption of atomic H is neglected because its timescale is generally longer than the timescale for thermal hopping.

atoms/molecules, surface temperature, and the surface composition. The temperature of atomic H (and H₂) deposited on the ASW was 100 K in the experiments (Oba et al. 2019; Nguyen et al. 2021). In our models, the sticking coefficient for atomic H is taken from Dupuy et al. (2016), who determined the sticking coefficient for atomic H on ASW for various incident kinetic energies and surface temperatures on the basis of classical molecular dynamics (MD) simulations. In our models, the sticking coefficient is set to 0.65 at $T_s = 10$ K, and 0.6 at 20 K and 30 K. These sticking coefficients are used in both cases where atomic H lands on empty sites (i.e., H₂O) and cases where H lands on either H₂S or PH₃. The sticking coefficient for H₂ is assumed to be the same as that for atomic H.

2.2.2. Binding energy

Amiaud et al. (2006, 2015) constrained the binding energy distribution of H₂ on porous ASW on the basis of temperature-programmed desorption (TPD) experiments. They found that the binding energy distribution can be described by a polynomial function, adopting $\nu_{\text{des}} = 1.8 \times 10^{12} \text{ s}^{-1}$ (Amiaud et al. 2015):

$$g_{\text{H}_2}(E_b) = \begin{cases} a(E_b^{\text{max}} - E_b)^{1.6} & (E_b^{\text{min}} \leq E_b < E_b^{\text{max}}) \\ 0 & (\textit{otherwise}) \end{cases} \quad (9)$$

where $a = 4.7 \times 10^{11} \text{ sites cm}^{-2} \text{ meV}^{-2.6}$ and $E_b^{\text{max}} = 67.5 \text{ meV}$ ($\sim 780 \text{ K}$) (Amiaud et al. 2015). Notably, the functional form of g_{H_2} indicates that the number of adsorption sites with smaller E_b is greater. The lower bound of E_b (E_b^{min}) was not constrained well by the TPD experiments because H₂ was deposited on ASW at a surface temperature of 10 K; even if adsorption sites with very low E_b exist, they would not be probed by the TPD experiments because of efficient thermal desorption even at 10 K. For example, the timescale of thermal desorption from sites with $E_b = 250 \text{ K}$ is only $\sim 0.1 \text{ s}$ at 10 K. The minimum value of E_b constrained by their experiments was $\sim 30 \text{ meV}$ ($\sim 350 \text{ K}$) (Amiaud et al. 2006); however, we extrapolate $g_{\text{H}_2}(E_b)$ to lower E_b . In the present work, E_b^{min} is treated as a free parameter and we test three values: $E_b^{\text{min}} = 150 \text{ K}$, 250 K , and 350 K . According to the numerical investigation of Molpeceres & Kästner (2020), who used MD simulations, approximately 75% of the adsorption sites for H₂ on ASW have an E_b in the range between 150 K and 450 K and sites with even lower E_b exist, although the peak binding energy distribution is $\sim 300 \text{ K}$ in their simulations. Because the intermolecular potential energy of a H₂-H₂O dimer is $\sim 120 \text{ K}$ (Zhang et al. 1991), the model with $E_b^{\text{min}} = 150 \text{ K}$ corresponds to the situation where the majority of sites have an E_b as low as the intermolecular energy of a dimer. We also tested some models in which the binding energy distributions for H₂ (and atomic H) follow a Gaussian distribution, but found no clear advantage over using a polynomial distribution (see Appendix for details). The cumulative distribution for the H₂ binding energy is shown in Fig. 3.

The atomic H binding energy obtained from experiments is not well constrained because of the high reactivity of atomic H. In this work, we assume that the binding energy of atomic H is given by $fE_b(\text{H}_2)$, where f is a scaling factor. Wakelam et al. (2017) have reported that the binding energy of stable molecules on ASW, as determined from TPD experiments, is proportional to the intermolecular potential energy between a dimer of

the molecule and H₂O (see their Fig. 1). The intermolecular energy between a dimer of atomic H and H₂O is $\sim 70 \text{ K}$, whereas that between a dimer of H₂ and H₂O is $\sim 120 \text{ K}$ (Zhang et al. 1991) (i.e., the former is ~ 0.6 times smaller than the latter). We varied f in the range $0.6 \leq f \leq 1.0$ in the present work. The cumulative distribution of the atomic H binding energy is shown by red lines in Fig. 3. Notably, the binding energy distribution for atomic H in our models is controlled by two independent parameters: $E_b^{\text{min}}(\text{H}_2)$ and f . The former parameter controls the extent of $E_b(\text{H})$, whereas the latter parameter controls the maximum value of $E_b(\text{H})$, which is given by $fE_b^{\text{max}}(\text{H}_2)$. Notably, we assume that the presence of H₂S or PH₃ does not affect the binding energies of atomic H and H₂ on porous ASW.

At the beginning of each kMC simulation, $E_b(\text{H}_2)$ at each lattice site is assigned randomly, but it follows g_{H_2} . The $E_b(\text{H})$ at each lattice site is set to $fE_b(\text{H}_2)$; that is, H₂ and atomic H share adsorption sites and shallow (deep) potential sites for H₂ are also shallow (deep) for atomic H.

According to TPD experiments, the binding energy of H₂S on water ice is 2700 K (Collings et al. 2004; Garrod & Herbst 2006; Jiménez-Escobar & Muñoz Caro 2011). To the best of our knowledge, no experimental measurements of the binding energy of HS, PH₃, or PH₂ on water ice have been reported. However, theoretically calculated binding energies for HS, PH₃, or PH₂ on water ice are available: 2700 K for HS (Wakelam et al. 2017), 2200 K for PH₃, and 1800 K for PH₂ (mean values; Molpeceres & Kästner 2021). Sil et al. (2021) and Nguyen et al. (2021) also calculated the binding energy of PH₃ on water ice and reported a value similar to that of Molpeceres & Kästner (2021). In our model, we neglect thermal desorption and thermal hopping of H₂S, HS, PH₃, and PH₂. Given the relatively high binding energy of these molecules, this assumption should be valid under the experimental conditions ($T_s \leq 30 \text{ K}$).

The integration of $g_{\text{H}_2}(E_b)$ from E_b^{max} to E_b^{min} gives the site density (N_{site}) on porous ASW. The N_{site} on porous ASW is known to be greater than that on flat crystalline water ice ($10^{15} \text{ molecules per cm}^2$) (Kimmel et al. 2001; Hidaka et al. 2008). N_{site} is $\sim 6 \times 10^{15}$, $\sim 4 \times 10^{15}$, and $\sim 2 \times 10^{15} \text{ sites cm}^{-2}$ when $E_b^{\text{min}} = 150 \text{ K}$, 250 K , and 350 K , respectively. We use different number of grids to unify the resolution of our models; n is determined to satisfy the relation, $N_{\text{site}}/(n \times n) \approx 2 \times 10^{11} \text{ sites cm}^{-2}$. In the models with $E_b^{\text{min}} = 150 \text{ K}$, 250 K , and 350 K , we use 161×161 , 128×128 , and 98×98 square lattices, respectively.

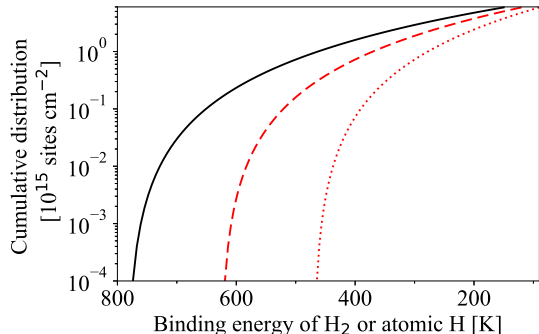


Figure 3. Cumulative distribution of the H₂ binding energy adopted in the present work (black line). Note that the minimum value of E_b for H₂ is treated as a free parameter. The red dashed line and the red dotted lines represent the cumulative distribution of the binding energy for atomic H in models with $f = 0.8$ and $f = 0.6$, respectively. When $f = 1.0$, the binding energy distribution for atomic H is identical to that for H₂. See the text for details.

In the experiments performed by Oba et al. (2019), 7×10^{14} molecules cm^{-2} of H₂S were deposited on ASW. In this case, the initial surface coverage of H₂S ($7 \times 10^{14}/N_{\text{site}}$) is $\sim 12\%$, $\sim 18\%$, and $\sim 35\%$ in our models with $E_b^{\text{min}} = 150$ K, 250 K, and 350 K, respectively. The initial positions of H₂S molecules on the grid are randomly determined at the beginning of each simulation.

2.2.3. Chemical desorption probability

The chemical desorption probabilities per reaction event for Reaction 1 (denoted as $P_{\text{cd}}(\text{H}_2\text{S})$) and for Reaction 3 ($P_{\text{cd}}(\text{PH}_3)$) are treated as free parameters in the present work. In the experiments by Oba et al. (2018, 2019), it was not possible to distinguish between the chemical desorption of H₂S upon Reaction 1 and the chemical desorption of HS upon Reaction 2. If the ratio of the binding energy of a reaction product to the energy released by the reaction is a key parameter for determining P_{cd} (e.g., Garrod et al. 2007; Minissale et al. 2016), then the P_{cd} for the hydrogenation reactions would be greater than those for the hydrogen abstraction reactions (see Table 1). In the present work, the P_{cd} of HS upon Reaction 2 ($P_{\text{cd}}(\text{HS})$) is always set to be lower than the $P_{\text{cd}}(\text{H}_2\text{S})$ by a factor of 10. Notably, our model results do not depend on the ratio of $P_{\text{cd}}(\text{HS})$ to $P_{\text{cd}}(\text{H}_2\text{S})$ but do depend on their sum because the chemical desorption of H₂S and HS occurs via the loop of Reactions 1 and 2. Similarly, the P_{cd} of PH₂ for Reaction 4 ($P_{\text{cd}}(\text{PH}_2)$) is set to be lower than that for Reaction 3 ($P_{\text{cd}}(\text{PH}_3)$) by a factor of 10. Throughout this work, P_{cd} is assumed to be independent of both T_s and the adsorption sites.

Table 2. Free parameters for the kinetic Monte Carlo simulations

Parameter	Values
$E_b^{\text{min}}(\text{H}_2)^{\text{a}}$	150 K (161 ²) - 250 K (128 ²) - 350 K (98 ²)
f	0.6 - 0.7 - 0.8 - 0.85 - 1.0
P_{cd}	1 % - 2 % - 3 % - 5 % - 10 % - 20 %

NOTE—^a The values in parentheses are the number of grids used in models with different $E_b^{\text{min}}(\text{H}_2)$ value.

For simplicity, we assume that P_{cd} of H₂, which can be formed by the recombination of H atoms and the hydrogen abstraction reactions, is unity. This assumption does not affect our results because H₂ can be directly adsorbed on the surface and because the flux of H₂ is as high as that of H atoms; the maximum formation rate of H₂ on the surface (i.e., one-half of the adsorption rate of atomic H) is comparable to the adsorption rate for H₂. Thus, the main source of H₂ on the surface is direct adsorption.

Our model has the three free parameters (i.e., $E_b^{\text{min}}(\text{H}_2)$, f , and P_{cd}); they are summarized in Table 2. In total, we ran 90 different models in which the three free parameters were varied. For each model, we ran the simulations five times with different random seeds and then took an average to reduce fluctuations in the calculation results. We then found the best “by-eye” fit model among the models. This model was considered to be the best fit to the experiments.

3. RESULTS

3.1. H₂S + H

3.1.1. Fiducial model

We first consider the results from one specific model to understand how the binding energy distribution affects the surface chemistry. The left panel of Figure 4 shows the H₂S abundance on ASW normalized by the initial H₂S abundance as a function of the H-atom exposure time in the model with $E_b^{\text{min}}(\text{H}_2) = 150$ K, $f = 0.85$, and $P_{\text{cd}}(\text{H}_2\text{S}) = 3\%$ (hereafter referred to as the fiducial model). The results show that $\sim 30\%$ of H₂S is lost within the first 1 min in the model at 10 K, which is clearly inconsistent with the experiments. Although the decrease in the H₂S abundance at later times ($\gtrsim 1$ min) is due to chemical desorption, this rapid loss of H₂S is not due to chemical desorption; as a result of the loop of H₂S–HS interconversion via Reactions 1 and 2, the abundance of H₂S decreases, whereas the abundance of HS increases. At $T_s = 10$ K, the probability

that Reaction 1 occurs per encounter of atomic H with H₂S is unity (i.e., $p_{\text{H}_2\text{S}+\text{H}} = 1$ and the reaction is effectively barrierless) when $E_{\text{hop}}(\text{H}) \gtrsim 150$ K (see Fig. 2). Because both Reactions 1 and 2 are (effectively) barrierless in sites with $E_{\text{hop}}(\text{H}) \gtrsim 150$ K, the abundances of HS and H₂S become similar as a result of the H₂S–HS interconversion in these sites (Fig. 5). This H₂S–HS interconversion should occur before substantial amounts of H₂S and HS are released from the surface by chemical desorption as long as $P_{\text{cd}}(\text{H}_2\text{S}) \ll 1$. Indeed, this rapid destruction and formation of H₂S and HS, respectively, via H₂S–HS interconversion are observed in all our models at 10 K, irrespective of the values of $E_{\text{b}}^{\text{min}}(\text{H}_2)$, f , and $P_{\text{cd}}(\text{H}_2\text{S})$. The degree of H₂S loss depends on the binding energy distribution of atomic H (i.e., the fraction of sites with $E_{\text{hop}}(\text{H}) \gtrsim 150$ K); however, more than 20% of the initial amount of H₂S is converted to HS within 1 min in all of our models at 10 K.

We conclude that the rapid destruction and formation of H₂S and HS, respectively, via H₂S–HS interconversion is inevitable at 10 K. In principle, if all adsorption sites have $E_{\text{hop}}(\text{H}) \ll 150$ K ($E_{\text{b}}(\text{H}) \ll 230$ K as $E_{\text{hop}}(\text{H}) \sim 0.65E_{\text{b}}(\text{H})$), then the abundance of HS would be negligible because $p_{\text{H}_2\text{S}+\text{H}} \ll 1$ for all sites, and the HS/H₂S abundance ratio would therefore be much lower than unity at 10 K (see Figure 5). In such models, however, reproducing the results of the experiments at 20 K and 30 K is difficult because efficient thermal desorption (e.g., the resident time of atomic H on the surface would be $<10^{-7}$ s at 20 K and even shorter at 30 K) prevents the occurrence of Reaction 1 and the chemical desorption of H₂S and HS would be negligible in the experimental timescale. The rapid destruction and formation of H₂S and HS, respectively, observed in the model at 10 K becomes much less obvious in the models at 20 K and 30 K (left panel of Fig. 4) because the thermal hopping rate of atomic H increases exponentially with increasing T_s . Thus, $p_{\text{H}_2\text{S}+\text{H}}$ is much less than unity for the majority of the adsorption sites; i.e., the HS/H₂S abundance ratio $\approx p_{\text{H}_2\text{S}+\text{H}} \ll 1$.

Oba et al. (2019) confirmed the chemical desorption of H₂S (and HS) by both FTIR spectroscopy in atomic H deposition experiments and QMS measurements in TPD experiments after H-atom deposition. During H-atom deposition, a decrease was observed in the magnitude of the band at 2570 cm⁻¹, which was assigned to an S–H stretching band of H₂S. However, distinguishing between H₂S and HS by FTIR is difficult because of overlap of the absorption bands (Jiménez-Escobar & Muñoz Caro 2011). In the TPD experiments after H-atom deposition, a decrease in the H₂S amount compared with the initial H₂S amount de-

posited on the ASW surface was found by QMS. The QMS measurements confirmed that no S-bearing species except H₂S were desorbed; however, both H₂S⁺ and HS⁺ were produced as fragment ions of H₂S, which could mask the existence of HS. Thus, we cannot rule out the possibility that some HS along with H₂S existed on the ASW in the experiments.

In the present work, as a working hypothesis, we interpret the 2570 cm⁻¹ band as the sum of the S–H stretching modes of H₂S and HS rather than solely as the stretching mode of H₂S. We also assume that the band intensity for H₂S and HS on ASW are the same because no literature value has been reported for HS. Under these assumptions, in the rest of this paper, we focus on the total abundance of S (i.e., H₂S + HS) on the ASW surface rather than the H₂S abundance in our simulations. In the right panel of Fig. 4, the vertical axis represents the total abundance of H₂S and HS normalized by the initial abundance of H₂S at a given time. In this case, we do not observe a rapid decrease at early times ($\lesssim 30$ s) at 10 K, whereas the results at 20 K and 30 K are similar between the two panels.

In the experiments, the abundance of H₂S (and HS) on ASW decreased with time and eventually became almost constant in the experimental timescale (Fig. 4). This nonlinear behavior reflects the binding energy distributions of atomic H and H₂ on ASW. Figure 6 shows the number of adsorption sites occupied by either H₂S or HS at $t = 0$ min (gray), 10 min (red), and 150 min (blue) in the fiducial model at $T_s = 10$ K (left), 20 K (middle), and 30 K (right) as functions of $E_{\text{b}}(\text{H})$. Because the surface coverage of H₂S is $\sim 12\%$ at $t = 0$ min (Section 2.2.2), the majority of adsorption sites are empty and these empty sites are not included in the figure. At 10 K and at $t = 150$ min, H₂S and HS are populating adsorption sites with binding energies $E_{\text{b}}(\text{H})$ following a bimodal distribution ($E_{\text{b}}(\text{H}) \lesssim 150$ K and $E_{\text{b}}(\text{H}) \gtrsim 400$ K). In the deep sites ($E_{\text{b}}(\text{H}) \gtrsim 450$ K, which corresponds to $E_{\text{b}}(\text{H}_2) \gtrsim 530$ K as $E_{\text{b}}(\text{H}) = 0.85E_{\text{b}}(\text{H}_2)$ in the fiducial model), H₂S and HS are buried by H₂; because H₂ does not easily hop to neighboring sites, further reactions of H₂S and HS with atomic H are hindered, as described in Section 2.1. The hopping timescale for H₂ from a site with $E_{\text{b}}(\text{H}_2) = 530$ K to a site with $E_{\text{b}}(\text{H}_2) \lesssim 450$ K exceeds the duration of the experiments (150 min). In the shallow sites ($E_{\text{b}}(\text{H}) \lesssim 150$ K), $p_{\text{H}_2\text{S}+\text{H}}$ is less than unity, which slows the loop of H₂S–HS interconversion; the rate of the chemical desorption is thereby reduced. H₂S only in the sites with $E_{\text{b}}(\text{H}) \lesssim 250$ K and $E_{\text{b}}(\text{H}) \lesssim 350$ K remains on the surface after 150 min at 20 K and 30 K, respectively. H₂ readily hops from the deepest sites to shallower sites and is thermally des-

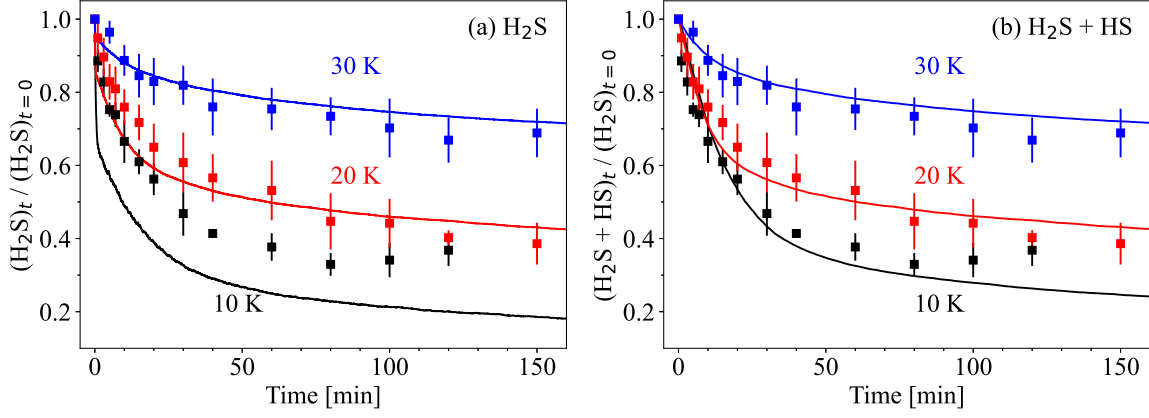


Figure 4. H₂S abundance (left panel) and total abundance of H₂S and HS (right panel) on ASW, normalized by the initial H₂S abundance and plotted as functions of the H-atom exposure time in the model with $E_b^{\text{min}}(\text{H}_2) = 150$ K, $f = 0.85$, and $P_{\text{cd}}(\text{H}_2\text{S}) = 3\%$ (lines). Square symbols represent experimental results reported by Oba et al. (2019) and based on FTIR spectroscopy. Black, red, and blue represent surface temperatures of 10 K, 20 K, and 30 K, respectively.

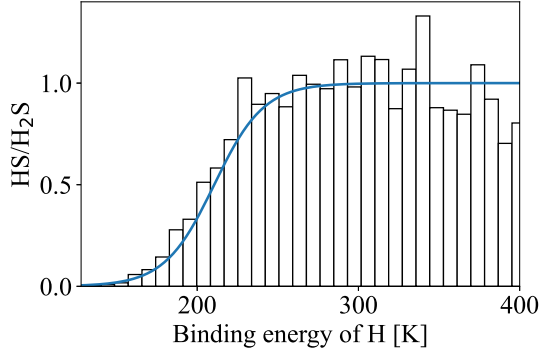


Figure 5. HS/H₂S abundance ratio in adsorption sites with different $E_b(\text{H})$ in the model with $E_b^{\text{min}}(\text{H}_2) = 150$ K, $f = 0.85$, and $P_{\text{cd}}(\text{H}_2\text{S}) = 3\%$ at $t = 1$ min (black bars). For comparison, $p_{\text{H}_2\text{S}+\text{H}}$ is shown as a blue line. In the evaluation of $p_{\text{H}_2\text{S}+\text{H}}$, $E_{\text{hop}}(\text{H})$ is assumed to be $0.65E_b(\text{H})$.

orbed at 20 K and 30 K; essentially no H₂ remains on ASW. A bimodal distribution is therefore not observed at 20 K and 30 K.

We can roughly estimate the threshold value of $E_b(\text{H})$ ($E_b^{\text{thresh}}(\text{H})$); most H₂S in sites with a binding energy lower than $E_b^{\text{thresh}}(\text{H})$ remains on ASW after 150 min of H-atom deposition, avoiding chemical desorption. The flux of H atoms is $5.7 \times 10^{13} \text{ cm}^{-2} \text{ s}^{-1}$ with a sticking probability of ~ 0.6 ; thus, the fluence (i.e., the time integral of the flux) of H atoms in 150 min is $\sim 3 \times 10^{17}$ molecules cm^{-2} . Because 7×10^{14} molecules cm^{-2} of H₂S are initially present on ASW, the average number of H atoms available to desorb one H₂S molecule via chemical desorption is ~ 400 . Let us assume that adsorbed H atoms are consumed either by the loop of Reactions 1–2 in sites with E_b or by thermal desorption. Under this assumption, the probability that Reaction 1 occurs before thermal desorption of a H atom is

given by $k_{\text{H}_2\text{S}+\text{H}} / (k_{\text{H}_2\text{S}+\text{H}} + k_{\text{des}}(\text{H}))$. Then, by solving $400[k_{\text{H}_2\text{S}+\text{H}} / (k_{\text{H}_2\text{S}+\text{H}} + k_{\text{des}}(\text{H}))]P_{\text{cd}}(\text{H}_2\text{S}) = 1$, we obtain $E_b^{\text{thresh}}(\text{H})$ to be ~ 100 K, 200 K, 300 K at $T_s = 10$ K, 20 K, and 30 K, respectively, when $P_{\text{cd}}(\text{H}_2\text{S}) = 3\%$. These values are consistent with the numerical results corresponding to $T_s = 20$ K and 30 K (see Fig. 6). In the numerical simulation at 10 K, H₂S and HS in adsorption sites even with $E_b(\text{H}) > E_b^{\text{thresh}}(\text{H})$ remain on the surface. The lack of agreement between the previously discussed simple argument and the numerical results at 10 K indicates the importance of trapping H atoms in deep-potential sites, followed by H₂ formation via recombination with another H atom. This effect can reduce the number of H atoms available for the H₂S–HS interconversion loop. Even for $E_b(\text{H}) = 660$ K (i.e., the deepest site), the timescale of hopping to a neighboring site is around 0.001 s at 20 K, which is comparable to the average adsorption timescale of one atomic H in our model, and the hopping timescale is even shorter at 30 K. Then the trapping of atomic H in deep sites is only important at 10 K.

Taken together, the nonlinear behavior of the total abundance of H₂S and HS on ASW can be understood as follows: At early times ($\lesssim 10$ min), chemical desorption occurs at adsorption sites, where the loop of H₂S–HS interconversion can occur most efficiently (i.e., $p_{\text{H}_2\text{S}+\text{H}} \sim 1$). At later times, the rate of chemical desorption is reduced, because the remaining H₂S is in sites less favorable for the H₂S–HS interconversion loop; that is, either $p_{\text{H}_2\text{S}+\text{H}} < 1$ or H₂S is buried by H₂, hindering further reactions. Eventually, H₂S only in sites with $E_b(\text{H})$ lower than $E_b^{\text{thresh}}(\text{H})$ remains on the ASW. At 10 K, H₂S (and HS) also remain in deep-potential sites, where the presence of H₂ hinders surface reactions.

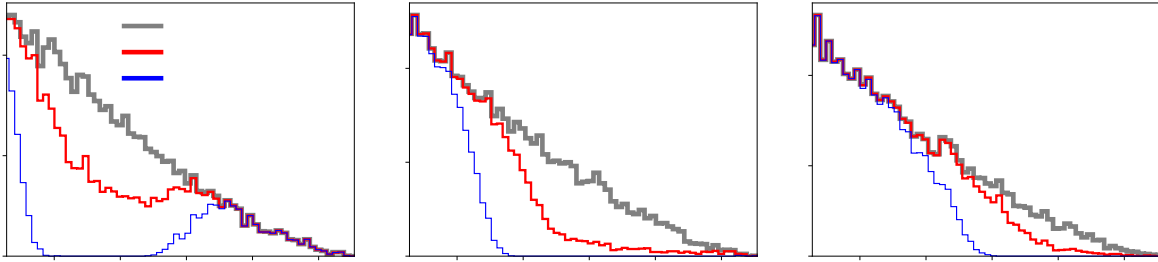


Figure 6. Number of adsorption sites occupied by either H₂S or HS at $t = 0$ min (gray), at 10 min (red), and at 15 min (blue) in the models with $f = 0.85$, $E_b^{\min} = 150$ K, and $P_{cd}(\text{H}_2\text{S}) = 3\%$ as functions of the binding energy of atomic H in the adsorption sites. The left, middle, and right panels show the model for a surface temperature of 10 K, 20 K, and 30 K, respectively. Note that the majority of adsorption sites are empty and that these empty sites are not included in the figure.

The previous discussion reveals that the binding energy distribution for atomic H can be directly constrained on the basis of the 20 K and 30 K experiments because the fraction of H₂S remaining on the ASW corresponds to the fraction of adsorption sites with $E_b(\text{H})$ lower than $E_b^{\text{thresh}}(\text{H})$. As previously mentioned, $E_b^{\text{thresh}}(\text{H})$ is ~ 200 K and 300 K at $T_s = 20$ K and 30 K, respectively. $E_b^{\text{thresh}}(\text{H})$ depends logarithmically on $P_{cd}(\text{H}_2\text{S})$; i.e., the dependence of $E_b^{\text{thresh}}(\text{H})$ on $P_{cd}(\text{H}_2\text{S})$ is weak. The abundance of H₂S becomes $\sim 40\%$ and $\sim 70\%$ of the initial H₂S abundance at 150 min in the 20 K and 30 K experiments, respectively. Thus, $\sim 70\%$ of the adsorption sites on porous ASW should have $E_b(\text{H}) \lesssim 300$ K, whereas $\sim 40\%$ of the adsorption sites should have $E_b(\text{H}) \lesssim 200$ K. Hama et al. (2012) found in their experiments that adsorption sites for atomic H on the ASW surface can be categorized into three groups: shallow ($E_{\text{hop}}(\text{H}) < 18$ meV ~ 210 K), middle ($E_{\text{hop}}(\text{H}) = 22$ meV ~ 260 K), and deep ($E_{\text{hop}}(\text{H}) > 30$ meV ~ 350 K) potential sites. Although the fraction of each of the three sites was not constrained well in their work, the shallow sites were found to be dominant on the surface. If we assume a hopping-to-binding energy ratio of 0.65 (Asgeirsson et al. 2017), the binding energy distribution constrained as previously described indicates that $\sim 70\%$ of the adsorption sites have $E_{\text{hop}}(\text{H}) \lesssim 0.65 \times 300 \sim 200$ K, consistent with the diffusion barriers constrained by Hama et al. (2012).

3.1.2. Lower limit of H₂S desorption probability

As previously discussed, the initial decrease of the H₂S and HS abundances at $\lesssim 10$ min in the experiments is likely due to chemical desorption from adsorption sites, where $p_{\text{H}_2\text{S}+\text{H}} = 1$ and, thus, the loop of H₂S–HS interconversion can occur most efficiently. We expect that reproducing the experimental results at $\lesssim 10$ min using models would be easier than reproducing the experimental results at > 10 min, where chemical desorption occurs even in sites with $p_{\text{H}_2\text{S}+\text{H}} < 1$. Thus, as a first step, attempting to constrain the $P_{cd}(\text{H}_2\text{S})$ while focusing only

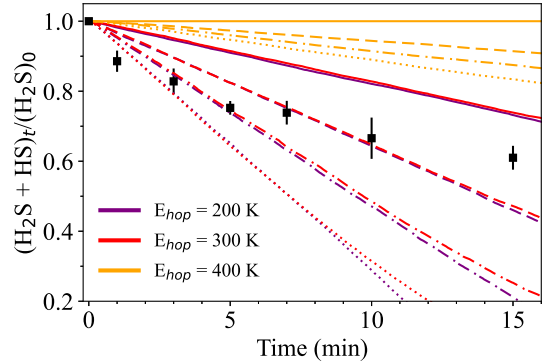


Figure 7. Temporal evolution of the H₂S abundance in the model with a single value of $E_{\text{hop}}(\text{H})$ at 10 K. Solid, dashed, dash-dotted, and dotted lines represent the models with $P_{cd}(\text{H}_2\text{S})$ of 1%, 2%, 3%, and 4%, respectively. The models with different $E_{\text{hop}}(\text{H})$ are represented in different colors. In all the models, thermal desorption of atomic H is neglected. Black squares show the experimental data (Oba et al. 2019).

on the experimental results at $\lesssim 10$ min would be worthwhile. For this purpose, we additionally ran models with a single value of $E_{\text{hop}}(\text{H})$ for all adsorption sites. We varied $E_{\text{hop}}(\text{H})$ in the range where $p_{\text{H}_2\text{S}+\text{H}} = 1$ (i.e., $E_{\text{hop}}(\text{H}) > 150$ K at $T_s = 10$ K). In these models, we neglected thermal desorption of atomic H for simplicity, whereas we considered H₂ formation by recombination of two H atoms. The other parameters were the same as those described in Section 2.2. We here focus on the 10 K experiments because thermal desorption of atomic H should occur efficiently at 20 K and 30 K, invalidating the aforementioned assumption.

Figure 7 shows the total abundance of H₂S and HS normalized by the initial H₂S abundance as functions of the H-atom exposure time at 10 K, where $E_{\text{hop}}(\text{H})$ and $P_{cd}(\text{H}_2\text{S})$ were varied. When $E_{\text{hop}}(\text{H}) = 400$ K or larger, $E_{\text{hop}}(\text{H})$ and $P_{cd}(\text{H}_2\text{S})$ degenerate (i.e., we cannot constrain $P_{cd}(\text{H}_2\text{S})$). However, when $E_{\text{hop}}(\text{H}) = 200$ K and 300 K, the results do not depend on $E_{\text{hop}}(\text{H})$ but do depend on $P_{cd}(\text{H}_2\text{S})$ because the diffusion of H atoms by

thermal hopping is fast and almost all the adsorbed H atoms are consumed by either Reaction 1 or Reaction 2 before another H atom is adsorbed onto the ASW surface. That is, Reactions 1 and 2 are adsorption-limited and the number of H₂S and HS released from the surface is simply given by $P_{\text{cd}}(\text{H}_2\text{S})$ multiplied by the number of adsorbed H atoms. In the experiments, some adsorbed H atoms might have been trapped in deep-potential sites and/or desorbed thermally; these effects are not included in the models with a single value of E_{hop} but indeed occur in the models where the binding energy distribution is taken into account. Then, what we can constrain here is the lower limit of $P_{\text{cd}}(\text{H}_2\text{S})$ by comparing the models with $E_{\text{hop}} \leq 300$ K with the experiments at $t \lesssim 10$ min. If we consider the experimental results only at $t \leq 5$ min, the lower limit of $P_{\text{cd}}(\text{H}_2\text{S})$ is $\sim 3\%$. If we consider the experimental results at $t \leq 10$ min, the lower limit of $P_{\text{cd}}(\text{H}_2\text{S})$ is $\sim 2\%$. As a conservative choice, we consider the lower limit of $P_{\text{cd}}(\text{H}_2\text{S})$ as 2%.

3.1.3. Constraining the H₂S desorption probability

Figure 8 shows the total amount of H₂S and HS divided by the initial amount of H₂S at 10 K, 20 K, and 30 K as functions of the H-atom exposure time in the models with $P_{\text{cd}}(\text{H}_2\text{S}) = 2\%$, where the other free parameters, f and $E_{\text{b}}^{\text{min}}(\text{H}_2)$, were varied. The model results are sensitive to f and $E_{\text{b}}^{\text{min}}(\text{H}_2)$ at 20 K and 30 K, whereas the impact of the two parameters is less significant at 10 K. At 20 K and 30 K, H₂S and HS in adsorption sites with higher $E_{\text{b}}^{\text{min}}(\text{H})$ are preferentially lost from the surface (Fig. 6). Lower values of f and $E_{\text{b}}^{\text{min}}(\text{H}_2)$ lead to a decrease in the fraction of deeper sites. As a result, the chemical desorption rate is reduced with decreasing f and/or $E_{\text{b}}^{\text{min}}(\text{H}_2)$, as evident in Figure 8. At 10 K, H₂S and HS become populating adsorption sites with binding energies $E_{\text{b}}^{\text{min}}(\text{H})$ following a bimodal distribution (Fig. 6). Lower values of f and $E_{\text{b}}^{\text{min}}(\text{H}_2)$ lead to a decrease in the fraction of deep sites (i.e., the chemical desorption rate tends to increase), whereas they lead to an increase in the fraction of shallow sites (i.e., the chemical desorption rate tends to decrease). As a result, the 10 K model is less sensitive to f and $E_{\text{b}}^{\text{min}}(\text{H}_2)$ than the 20 K and 30 K models.

Because 2% is the lower limit of $P_{\text{cd}}(\text{H}_2\text{S})$, the models that overestimate the amount of H₂S and HS desorbed from the ASW surface compared to the experiments are ruled out. Examining the 20 K and 30 K models, we can rule out the majority (6 of 9) of the models shown here. The three models not yet ruled out are those with $E_{\text{b}}^{\text{min}}(\text{H}_2) = 250$ K and $f = 0.6$, with $E_{\text{b}}^{\text{min}}(\text{H}_2) = 150$ K and $f = 0.6$, and with $E_{\text{b}}^{\text{min}}(\text{H}_2) = 150$ K and $f = 0.8$

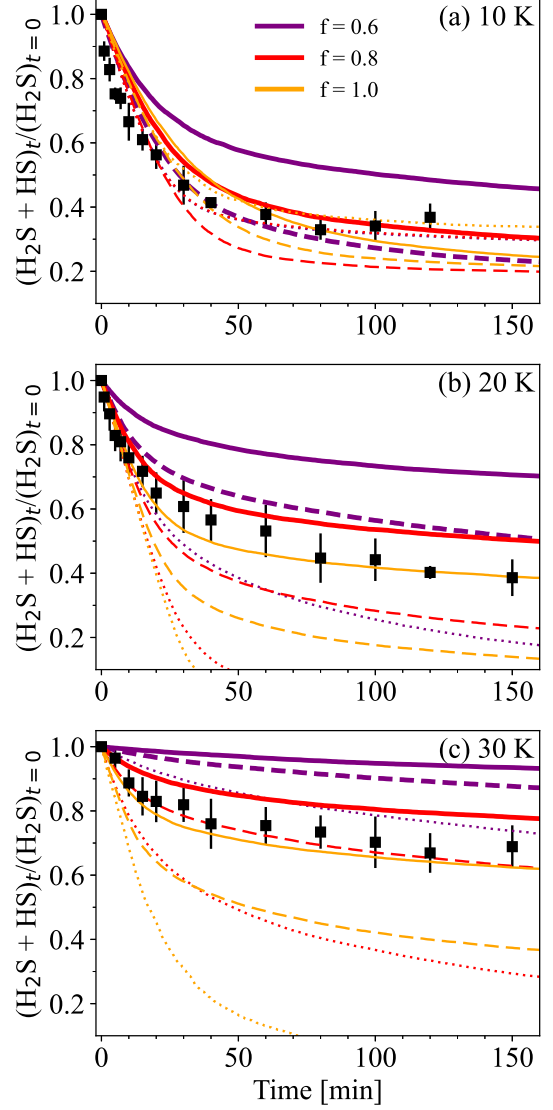


Figure 8. Total S (H₂S + HS) abundance with respect to the initial H₂S abundance on porous ASW at 10 K (panel a), 20 K (panel b), and 30 K (panel c) as functions of the H-atom exposure time in the kMC simulations (lines) and in the experiments by Oba et al. (2019) (black squares). Solid, dashed, and dotted lines represent the models with $E_{\text{b}}^{\text{min}}(\text{H}_2)$ values of 150 K, 250 K, and 350 K, respectively. The models with different $E_{\text{hop}}(\text{H})$ values are represented in different colors. In all the simulations, $P_{\text{cd}}(\text{H}_2\text{S})$ is set to 2%.

(shown by thick lines in Fig. 8). Notably, the three models share the common feature of a low atomic H binding energy; more than one-half of the adsorption sites have a low binding energy for atomic H ($\lesssim 300$ K, see Fig. 3) and, thus, a low hopping barrier ($\lesssim 200$ K).

Among the three models, we disfavor the model with $E_{\text{b}}^{\text{min}}(\text{H}_2) = 250$ K and $f = 0.6$ because, although the model moderately well reproduces the experimental results at $T_s = 10$ K, too much H₂S and HS remain on

the surface at 30 K compared to the experiments; the experiments at 10 K, 20 K, and 30 K are difficult to fit simultaneously by varying $P_{\text{cd}}(\text{H}_2\text{S})$. We thus have two remaining possibilities: (i) the model with $f = 0.6$ and $E_{\text{b}}^{\text{min}}(\text{H}_2) = 150$ K is more favorable and $P_{\text{cd}}(\text{H}_2\text{S})$ is much higher than the lower limit value of 2% because too much H_2S and HS remains on the surface compared with the experiments at all the investigated temperatures, or (ii) the model with $f = 0.8$ and $E_{\text{b}}^{\text{min}}(\text{H}_2) = 150$ K is more favorable and $P_{\text{cd}}(\text{H}_2\text{S})$ is close to and slightly greater than 2% because the model somehow underestimates chemical desorption at all the investigated temperatures.

To explore the first possibility, we tested additional models, varying f from 0.6 to 0.8 and varying $P_{\text{cd}}(\text{H}_2\text{S})$ from 5% to 20% but fixing $E_{\text{b}}^{\text{min}}(\text{H}_2) = 150$ K. The results for these models are shown in Fig. 13 in the appendix. We find that reproducing the 10–30 K experiments simultaneously using these models with a relatively high $P_{\text{cd}}(\text{H}_2\text{S})$ of $>5\%$ is difficult; the models at 10 K overestimate the amount of H_2S and HS desorbed from the surface compared with the experiments, or the models at 30 K underestimate the amount of H_2S and HS desorbed from the surface compared with the experiments.

Therefore, we conclude that the second possibility is more favorable; i.e., the $P_{\text{cd}}(\text{H}_2\text{S})$ is close to the lower limit value of 2%. After some exploration, we found that the model with $f = 0.85$, $E_{\text{b}}^{\text{min}}(\text{H}_2) = 150$ K, and $P_{\text{cd}}(\text{H}_2\text{S}) = 3\%$ (i.e., the fiducial model) reasonably well reproduces the 10 K, 20 K, and 30 K experimental results simultaneously (see the right panel of Fig. 4). We confirmed that the reduced χ^2 for this model ($= 1.85$) is the minimum among all the models applied in the present work. We consider this model as the best-fit model.

As noted in Section 2.2.3, our model results depend on the sum of $P_{\text{cd}}(\text{H}_2\text{S})$ and $P_{\text{cd}}(\text{HS})$, but do not depend on the ratio of $P_{\text{cd}}(\text{HS})$ to $P_{\text{cd}}(\text{H}_2\text{S})$, which is assumed to be 0.1 throughout the present work. Thus, strictly speaking, the constraint applied here is that the sum of $P_{\text{cd}}(\text{H}_2\text{S})$ and $P_{\text{cd}}(\text{HS})$ is 3.3%. Nevertheless, $P_{\text{cd}}(\text{H}_2\text{S})$ can be reasonably expressed as $\sim 3\%$ because $P_{\text{cd}}(\text{H}_2\text{S})$ would be greater than $P_{\text{cd}}(\text{HS})$ according to the theoretical models for chemical desorption (see Section 4.3). Finally, we also ran models in which the binding energy distributions of atomic H and H_2 are given by a Gaussian distribution rather than by a polynomial distribution; we found no clear advantage to using a Gaussian distribution (see the appendix).

Our best-fit model underestimates the total abundance of H_2S and HS remaining on the ASW surface at

10 K compared with the experiments, although it better reproduces the 20 K and 30 K experimental results. This underestimation might indicate that the presence of H_2 on the surface lowers the P_{cd} . The ASW surface is partly covered by H_2 at 10 K, whereas essentially no H_2 remains on the surface at 20 K and 30 K. Minissale & Dulieu (2014) found in their experiments that the chemical desorption probability of O_2 upon the reaction between two O atoms decreases with increasing coverage of O_2 on oxidized graphite. The presence of an adsorbed species might enhance the dissipation of the excess energy produced by chemical reactions, resulting in a lowering of the P_{cd} Minissale & Dulieu (2014). Such an effect of an adsorbed species (H_2 in our case) on the P_{cd} is not considered in our models.

3.2. Constraining the PH_3 desorption probability

We here constrain the P_{cd} for PH_3 upon Reaction 4. As previously described, the experiments of $\text{H}_2\text{S} + \text{H}$ at 10 K, 20 K, and 30 K are reasonably well reproduced by the model with $f = 0.85$ and $E_{\text{b}}^{\text{min}}(\text{H}_2) = 150$ K. Therefore, in this subsection, we fixed the parameters f and $E_{\text{b}}^{\text{min}}$ to these values. As in Section 3.1, we discuss the total amount of PH_3 and PH_2 on the surface divided by the initial amount of PH_3 , again because the rapid conversion of PH_3 to PH_2 is inevitable at $T_s = 10$ K in our models; the rate of Reaction 3 is even greater than that of Reaction 1 (Table 1). Figure 9 compares the experimental results with the model, where the $P_{\text{cd}}(\text{PH}_3)$ was varied. Notably, the H atom flux was approximately four times greater in the experiments involving $\text{PH}_3 + \text{H}$ (Nguyen et al. 2021) than in those involving $\text{H}_2\text{S} + \text{H}$ (Oba et al. 2019). We find that the model with $P_{\text{cd}}(\text{PH}_3) = 4\%$ reasonably well reproduced the experiments at 10 K.

4. DISCUSSION

4.1. Uncertainties in the flux of atomic H

Thus far, the flux of H atoms was set to $5.7 \times 10^{13} \text{ cm}^{-2} \text{ s}^{-1}$ and $2.2 \times 10^{14} \text{ cm}^{-2} \text{ s}^{-1}$ in the $\text{H}_2\text{S} + \text{H}$ model and in the $\text{PH}_3 + \text{H}$ model, respectively. These fluxes were estimated by Oba et al. (2019) and Nguyen et al. (2021). The authors did not discuss the uncertainties in the estimation of the atomic H flux in their experiments; however, empirically, the absolute uncertainties can be as large as 50% (private communication). Here, we explore how the flux uncertainty affects the constraints on P_{cd} .

We tested two additional models for the $\text{H}_2\text{S} + \text{H}$ system, varying the H atom flux. In one model, the H atom flux was set to $3.8 \times 10^{13} \text{ cm}^{-2} \text{ s}^{-1}$ (50% lower than the fiducial value); in the other model, it was $8.6 \times 10^{13} \text{ cm}^{-2}$

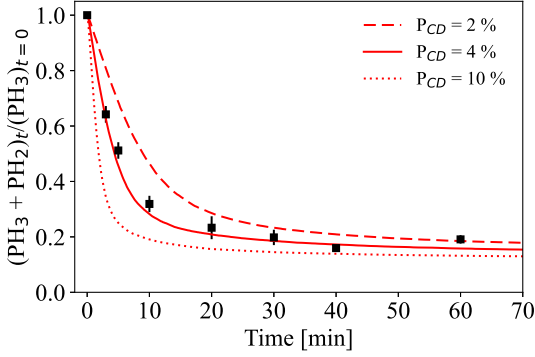


Figure 9. Relative abundances of phosphorous (PH₃ + PH₂) on porous ASW at 10 K as functions of the H-atom exposure time in the kMC simulations (lines) and in the experiments by Nguyen et al. (2021) (black squares). Solid, dashed, and dotted lines represent the models with $P_{cd}(\text{PH}_3)$ of 4%, 2%, and 10 %, respectively. In all the simulations, $E_b^{\min}(\text{H}_2)$ and f are set to 150 K and 0.85, respectively.

s^{-1} (50% higher). The other parameters were the same as in our fiducial model: $E_b^{\min}(\text{H}_2) = 150$ K, $f = 0.85$, and $P_{cd}(\text{H}_2\text{S}) = 3\%$. The model with the 50% lower H flux and $P_{cd}(\text{H}_2\text{S}) = 3\%$, and the model with the fiducial H flux and $P_{cd}(\text{H}_2\text{S}) = 1.5\%$ gave almost identical results, whereas the model with the 50% higher H flux and $P_{cd}(\text{H}_2\text{S}) = 3\%$ and the model with the fiducial H flux and $P_{cd}(\text{H}_2\text{S}) = 4.5\%$ gave almost identical results. Thus, the uncertainty in the H atom flux is inversely linearly transferred to the uncertainty in the $P_{cd}(\text{H}_2\text{S})$, likely because the system is adsorption-limited rather than diffusion-limited. Considering the empirical uncertainty in the H atom flux (50%), we conclude that the $P_{cd}(\text{H}_2\text{S})$ is $3 \pm 1.5\%$, whereas the $P_{cd}(\text{PH}_3)$ is $4 \pm 2\%$.

4.2. Diffusion of atomic H by quantum tunneling

In our fiducial models, thermal hopping is treated solely as a mechanism of surface diffusion. Asgeirsson et al. (2017) theoretically studied the diffusion of atomic H on amorphous ice, considering both thermal hopping and quantum tunneling, and showed that tunneling is important only for $T_s \lesssim 10$ K. Kuwahata et al. (2015) experimentally showed that tunneling dominates thermal hopping for atomic H on crystalline water ice at 10 K. However, tunneling is less important for the diffusivity of atomic H on ASW, where greater heterogeneity (i.e., a greater range in $E_b(\text{H})$) exists compared to the heterogeneity of crystalline water ice surfaces. The rationale is that, even though H atoms can tunnel between shallow sites, the rate-limiting step for long-range diffusion is the transition out of deep sites, which still requires thermal activation (Smoluchowski 1983; Kuwahata et al. 2015; Asgeirsson et al. 2017).

These experimental and theoretical studies indicate that tunneling has limited importance for long-range diffusion of atomic H on ASW at ≥ 10 K. On the other hand, tunneling diffusion might play a role in determining the reaction probability because it is determined by the competition between reaction and short-range diffusion (Eq. 8).

To check the effect of tunneling diffusion on our results, we tested additional models in which the tunneling diffusion of atomic H was considered. Lamberts et al. (2014) proposed tunneling rates for exothermic reactions based on arguments of microscopic reversibility. Because the diffusion rates should also obey microscopic reversibility, referring to Lamberts et al. (2014), we calculate the tunneling diffusion rates for atomic H between two sites with different binding energies ($E_b < E_{b'}$) as

$$k_{\text{diff,qt}}(E_b \rightarrow E_{b'}) = \nu \exp\left(-\frac{2d}{\hbar} \sqrt{2m_{\text{H}}\alpha E_b}\right), \quad (10)$$

$$\begin{aligned} & k_{\text{diff,qt}}(E_{b'} \rightarrow E_b) \\ &= k_{\text{diff,qt}}(E_b \rightarrow E_{b'}) \exp\left(-\frac{E_{b'} - E_b}{kT_s}\right), \quad (11) \end{aligned}$$

where surface sites are assumed to be separated by a rectangular barrier of thickness d and m_{H} is the mass of atomic H. Because the barrier thickness is unknown, we here consider two values: $d = 1$ Å and 2 Å. Notably, when atomic H moves from a deeper site to a shallower site, the part of activation energy barrier that corresponds to the difference in the binding energies of the two sites should be overcome thermally (see Fig. 1). This consideration is accounted for by the factor $\exp(-(E_{b'} - E_b)/kT_s)$ in Eq. 11. We compared the tunneling rate and thermal hopping rate and chose the higher of the two as the diffusion rate.

Figure 10 shows the effect of tunneling diffusion at $T_s = 10$ K when $d = 1$ Å (red solid line) and $d = 2$ Å (red dashed line). Compared with our best-fit model constrained as described in Section 3 (black solid line), tunneling increases the fraction of H₂S and HS released to the gas phase by chemical desorption to some extent. As a result, the model with tunneling diffusion underestimates the amount of H₂S and HS remaining on the ASW surface after 25 min compared with the experimentally observed amount. Even if we adopt $P_{cd}(\text{H}_2\text{S}) = 2\%$, which is the lower limit value, the model with tunneling underestimates the amount of H₂S and HS remaining on the ASW surface (blue lines). As discussed in Section 3.1.1, some H₂S and HS in sites with $E_b(\text{H}) > E_b^{\text{thresh}}(\text{H}) \sim 100$ K remain on the surface at 10 K in our fiducial model (see Fig. 6) because of trapping of H atoms in deep-potential sites, followed by the formation of H₂ via recombination with another H

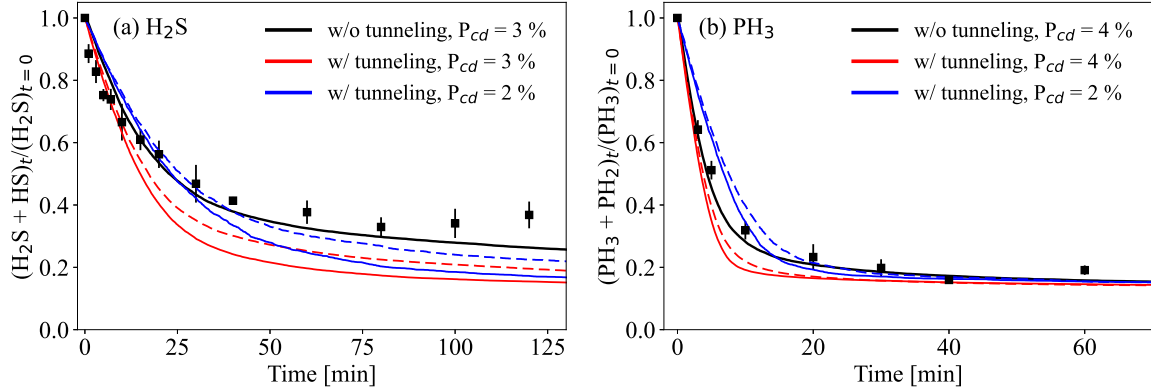


Figure 10. Total abundance of H₂S and HS (left panel) and total abundance of PH₃ and PH₂ as functions of the H atom exposure time in models with tunneling diffusion with a barrier thickness of 1 Å (red and blue solid lines) and in the models with tunneling diffusion with a barrier thickness of 2 Å (red and blue dashed lines) at 10 K. In all the models, $E_b^{\text{min}}(\text{H}_2) = 150$ K and $f = 0.85$. Our best-fit models constrained as described in Section 3 are shown by black solid lines for comparison. Square symbols represent the experimental results reported by Oba et al. (2019) and Nguyen et al. (2021).

atom. Because of the tunneling, the effect of trapping is reduced and almost all of the H₂S and HS in sites with $E_b(\text{H}) \sim 150$ K are released to the gas phase by chemical desorption in the model with tunneling diffusion. A similar effect is observed in the PH₃ + H model at 10 K. At 20 K and 30 K, the results obtained using the models with and without tunneling diffusion are almost identical (not shown).

When tunneling diffusion is considered, the model with $P_{\text{cd}}(\text{H}_2\text{S}) = 2\%$ better reproduces the H₂S + H experimental results at $T_s = 10$ K, 20 K, and 30 K rather than the model with $P_{\text{cd}}(\text{H}_2\text{S}) = 3\%$, assuming $E_b^{\text{min}}(\text{H}_2) = 150$ K and $f = 0.85$. Note, however, that the reduced χ^2 for this model is larger than that for our best-fit model constrained in Section 3 (~ 4 versus ~ 2). For the PH₃ + H system, the model with $P_{\text{cd}}(\text{H}_2\text{S}) = 3\%$ better reproduces experimental results rather than the model with $P_{\text{cd}}(\text{PH}_3) = 4\%$, when tunneling diffusion is considered. The reduced χ^2 for this model is similar to that for our best-fit model constrained in Section 3. Therefore, slightly lower P_{cd} than that constrained in Section 3 is favorable, when tunneling diffusion is considered.

4.3. Comparison with theoretical models of chemical desorption

Chemical desorption is caused by the energy released by reactions; after an exothermic surface reaction, some of the excess energy is dissipated into products' translational energy in the direction perpendicular to the surface, leading to desorption (e.g., Fredon et al. 2017). The efficiency of chemical desorption depends on (i) the excess energy released by reaction (E_{react}), (ii) the binding energy of products to the surface, (iii) the fraction of excess energy that remains in the products and is

not lost to the solid surface, and (iv) how the energy of the products is distributed among all degrees of freedom. The last two parameters are currently uncertain, which limits our quantitative understanding of chemical desorption. Several authors have suggested general formalisms of chemical desorption to be used in astrochemical models (Garrod et al. 2007; Minissale et al. 2016; Fredon et al. 2021). These formalisms include free parameters that should be determined by laboratory experiments or/and quantum chemistry calculations. Here, we compare the P_{cd} constrained in the present work with that predicted by the theoretical models of chemical desorption in the literature.

Garrod et al. (2007) proposed the following formalism in the case of one-product reactions, applying Rice–Ramsperger–Kessel–Marcus theory:

$$P_{\text{cd}, \text{G07}} = \frac{a\gamma}{1 + a\gamma}, \quad (12)$$

$$\gamma = \left(1 - \frac{E_b}{E_{\text{react}}}\right)^{s-1}, \quad (13)$$

where γ is the probability for an energy $E > E_b$ to be present in the admolecule–surface bond and s is the number of vibrational degrees of freedom, including binding to the surface. The parameter $a = \nu/\nu_s$ is the ratio of the desorption attempt frequency to the frequency at which the reaction energy is lost to the surface. The value of a is unknown, and $a = 0.01$ (i.e., $P_{\text{cd}, \text{G07}} \sim 1\%$) is often assumed in astrochemical models (e.g., Garrod et al. 2007; Taquet et al. 2014; Furuya et al. 2015). In the case of two-product reactions, chemical desorption is assumed to not occur (Garrod et al. 2007).

Minissale et al. (2016) proposed a different formulation from that of Garrod et al. (2007) to explain the re-

sults of their chemical desorption experiments. They treated the energy dissipation as an elastic collision, where some of the kinetic energy is transferred to the surface from the product species, and assumed that excess energy that remains in the product species is spread equally over all degrees of freedom of the product species. Their formulation with an effective surface mass of 130 amu reproduced the efficiency of chemical desorption for the studied reactions on graphite surfaces (i.e., rigid surfaces) within the margin of error. However, the use of the formulation by Minissale et al. (2016) is questionable for ASW surfaces, where intermolecular interactions dominate and the collisions between ad-molecules and the surface are inelastic (Fredon et al. 2017). Because our work is focused on chemical desorption on ASW, hereafter we do not discuss the formalism of Minissale et al. (2016).

More recently, Fredon et al. (2021) proposed the following formulation based on classical MD simulations, where excess energy is transferred to a molecule adsorbed on ASW and the fate of the molecule is tracked (see also Fredon et al. 2017):

$$P_{\text{cd, F21}} = \alpha \left(1 - \exp \left(-\frac{\chi E_{\text{react}} - E_{\text{b}}}{3E_{\text{b}}} \right) \right), \quad (14)$$

where α is an empirical factor of 0.5 and the factor of 3 in the denominator arises from the assumption that only translational excitation in the direction perpendicular to the surface can lead to desorption. The free parameter χ describes the fraction of excess energy transferred to the translational excitation of products. They proposed that χ depends on the number of product species; for product species i , χ is given by

$$\chi_i = \begin{cases} \chi_1 & \text{(one product reaction),} \\ \chi_2 \frac{m_j}{m_i + m_j} & \text{(two product reaction),} \end{cases} \quad (15)$$

where m_i is the mass of product species i , and m_j is the mass of another species produced by the reaction. Fredon et al. (2021) conducted gas-ice astrochemical simulations using the rate equation method in conjunction with their formalism and found that their model reasonably well reproduces the observations of gas-phase (complex) organic molecules in dark clouds when $\chi_1 = 0.1$. They also found that the gas-phase abundances of organic molecules are not sensitive to the choice of χ_2 because surface reactions that are efficient at low temperatures (~ 10 K) involve atomic H or H₂ and, thus, χ_i is small for organic molecules, which is more massive than atomic H and H₂.

Figure 11 compares P_{cd} for Reactions 2 and 4 constrained as described in the present work with those predicted from the formulations proposed by Fredon et al.

(2021) (left panel) and by Garrod et al. (2007) (right panel). The binding energy of H₂S and PH₃ was set to 2700 K and 2200 K, respectively (Collings et al. 2004; Molpeceres & Kästner 2021). The energy released by the reactions is listed in Table 1. The Fredon formulation predicts that $P_{\text{cd}}(\text{H}_2\text{S})$ should be lower than $P_{\text{cd}}(\text{PH}_3)$, whereas the Garrod formulation predicts the opposite trend. Our results indicate that $P_{\text{cd}}(\text{H}_2\text{S})$ is slightly lower than $P_{\text{cd}}(\text{PH}_3)$; thus, the Fredon formulation is more consistent with our findings. From a quantitative comparison, we find that the Fredon formulation with $\chi_1 \sim 0.07$ reproduces both $P_{\text{cd}}(\text{H}_2\text{S})$ and $P_{\text{cd}}(\text{PH}_3)$ constrained as described in the present work; i.e., approximately 7% of the excess energy is transferred to the translational excitation of the products. The Fredon formulation predicts that, even if χ_2 is unity, the values of $P_{\text{cd}}(\text{HS})$ and $P_{\text{cd}}(\text{PH}_2)$ are zero, adopting the HS and PH₂ binding energies at 2700 K and 1800 K, respectively. These results support our assumption that P_{cd} for the H addition reactions is higher than that for the H abstraction reactions. If we adopt the Garrod formulation to explain $P_{\text{cd}}(\text{H}_2\text{S})$ and $P_{\text{cd}}(\text{PH}_3)$, the parameter a should be ~ 0.05 , which is larger than the typically assumed value of 0.01.

Whether the Fredon formulation with $\chi_1 \sim 0.07$ provides reasonable estimates of P_{cd} for other reaction systems is unclear. Pantaleone et al. (2020) used ab initio MD simulations to study the fate of energy released by the reaction $\text{H} + \text{CO} \rightarrow \text{HCO}$ on crystalline water ice and found that 90% of the reaction energy is instantly injected toward the water ice. The fraction of excess energy transferred to the translational excitation should be less than 10% in this case. However, Pantaleone et al. (2021) studied the H₂ formation on water ice surfaces using ab initio MD simulations and found that as much as two-thirds of the reaction energy is injected toward the water ice and the remaining energy is retained in the produced H₂. Experimental and numerical studies of additional systems are required to draw any solid conclusions.

4.4. Astrochemical implications

Gaseous H₂S has been detected in various evolutionary stages of star and planet formation, cold dense clouds (e.g., Minh et al. 1989; Ohishi et al. 1992; Navarro-Almáida et al. 2020), envelope around protostars (e.g., Blake et al. 1994; Wakelam et al. 2004), and protoplanetary disks (Phuong et al. 2018; Rivière-Marichalar et al. 2021). The formation of H₂S in the gas phase is inefficient because of the presence of endothermic reactions in the sequence of reaction pathways to convert S⁺ or atomic S into H₂S (e.g.,

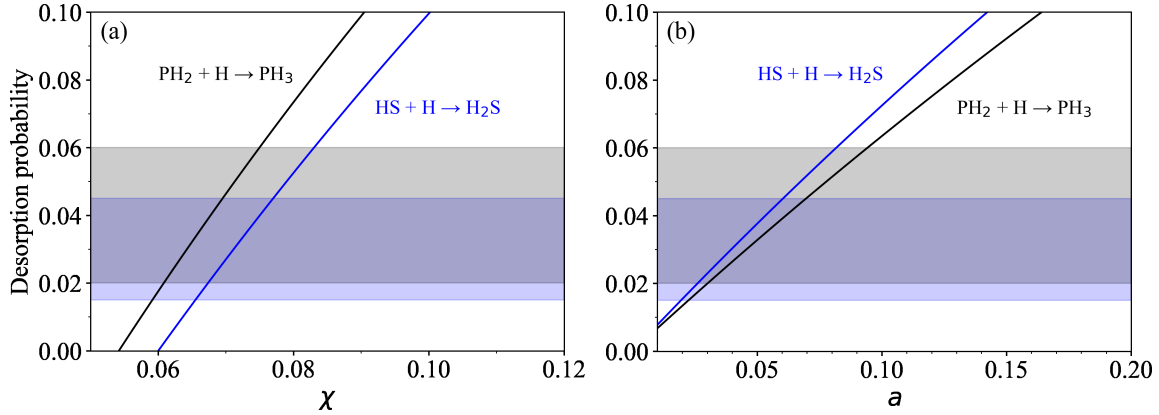


Figure 11. Chemical desorption probability of H_2S via Reaction 2 (blue line) and PH_3 via Reaction 4 (black line) predicted by the formulation of Fredon et al. (2021) (Eq. 14, panel a) and that by Garrod et al. (2007) (Eq. 13, panel b). $P_{\text{cd}}(\text{H}_2\text{S})$ and $P_{\text{cd}}(\text{PH}_3)$ constrained in the present work are shown by purple and gray areas, respectively.

Yamamoto 2017); the reaction of S^+ with H_2 to form SH^+ is endothermic, as is the reaction of SH^+ (which can be formed by the reaction between atomic S and H_3^+) with H_2 to form SH_2^+ . H_2S has been speculated to be produced on grain surfaces by the sequential hydrogenation of atomic S on grain surfaces and subsequently released to the gas phase by thermal or non-thermal desorption processes, the latter of which should dominate the former at low temperatures (~ 10 K) (e.g., Garrod et al. 2007). In the dark cloud L134N, the gas-phase H_2S abundance with respect to hydrogen nuclei is 4×10^{-10} (Ohishi et al. 1992). H_2S ice has not been detected in star-forming regions and the upper limit of the $\text{H}_2\text{S}/\text{H}_2\text{O}$ ice abundance ratio is $\sim 1\%$ (Smith 1991), corresponding to the H_2S ice abundance with respect to hydrogen nuclei of $\lesssim 10^{-6}$.

Very little is known about PH_3 in star-forming regions. Neither gas-phase nor solid-phase PH_3 has been detected in star-forming regions (e.g., Turner et al. 1990; Lefloch et al. 2016). Like the gas-phase formation of H_2S , the formation of PH_3 via gas-phase reactions is inefficient (Thorne et al. 1984). Thus, the main formation pathway for gas-phase PH_3 is the formation of PH_3 ice by the sequential hydrogenation of atomic P on grain surfaces, followed by thermal or nonthermal desorption, as assumed in previous astrochemical models (e.g., Charnley & Millar 1994; Aota & Aikawa 2012; Chantzos et al. 2020; Sil et al. 2021).

To explore the effect of the chemical desorption of H_2S and PH_3 on their gas-phase abundances, we conducted gas–ice astrochemical simulations using the modified rate-equation method (Garrod 2008) under dark-cloud physical conditions; the number density of hydrogen nuclei (n_{H}), the temperature, and the visual extinction were set to $2 \times 10^4 \text{ cm}^{-3}$, 10 K, and 10 mag, respectively. The cosmic-ray ionization rate of H_2 was set to

$1.3 \times 10^{-17} \text{ s}^{-1}$. In our rate-equation model, the chemistry is described by a three-phase model, where the gas phase, a surface of ice, and the chemically inert bulk ice mantle are considered (Hasegawa & Herbst 1993). As nonthermal desorption processes, which are relevant to H_2S and PH_3 , chemical desorption and photodesorption were considered. The chemical desorption probability for reactions other than Reactions 2 and 4 were calculated using the method of Garrod et al. (2007), assuming $a = 0.01$. The photodesorption yields per incident far-ultraviolet (FUV) photons of H_2S and PH_3 were set to 10^{-3} (see Fuente et al. 2017). Additional details can be found in Furuya et al. (2015); Furuya & Persson (2018).

Although our kMC simulations have shown that the distribution of adsorption sites with different potential-energy depths plays a role in the chemical desorption of H_2S and PH_3 , we must choose single values for the binding energy and the hopping energy of atomic H in the rate-equation model. We set the hopping energy of atomic H to be 80 K, which corresponds to the low end of the distribution. The $p_{\text{H}_2\text{S}+\text{H}}$ was then 3×10^{-3} , and the $p_{\text{PH}_3+\text{H}}$ was 3×10^{-2} . The binding energy of atomic H was set to 300 K.

The amounts of elemental S and P available for gas and ice chemistry in the interstellar matter (ISM) are uncertain. In diffuse clouds, S is predominantly present in the gas phase, whereas P in the gas phase is depleted to some extent (Jenkins 2009). On the other hand, previous observations and modeling studies have suggested that the S and P abundances in star-forming regions are much lower than the values in diffuse clouds (e.g., Wakelam et al. 2004; Lefloch et al. 2016). A large fraction of elemental S and P might be incorporated into refractory compounds during the evolution from diffuse clouds to denser clouds (e.g., Bergner et al. 2019;

Cazaux et al. 2021). Here, we assume that the elemental abundances of S and P available for gas and ice chemistry in the dark-cloud stage are lower than those observed in diffuse clouds by a factor 100 (Graedel et al. 1982; Wakelam & Herbst 2008). The elemental abundances of S and P with respect to H were set to 1.5×10^{-7} and 1.2×10^{-9} , respectively. The elemental abundances of other elements were taken from Aikawa & Herbst (1999). Initially the species were assumed to be atoms or atomic ions except for hydrogen, which is in molecular form.

Figure 12 shows the temporal evolution of S-bearing species (left panel) and P-bearing species (right panel), where the $P_{\text{cd}}(\text{H}_2\text{S})$ and $P_{\text{cd}}(\text{PH}_3)$ were varied. In the model with $P_{\text{cd}}(\text{H}_2\text{S}) = P_{\text{cd}}(\text{PH}_3) = 0\%$, almost all the S and P are eventually confined in H₂S ice and PH₃ ice, respectively. The main production pathway for gas-phase H₂S and PH₃ is photodesorption of the corresponding icy molecules by cosmic-ray-induced FUV photons. In the model with $P_{\text{cd}}(\text{H}_2\text{S}) = 3\%$ and $P_{\text{cd}}(\text{PH}_3) = 4\%$, as constrained in the present work, the gas-phase abundances of H₂S and PH₃ are higher by orders of magnitude than those in the model with $P_{\text{cd}} = 0\%$. This result indicates that chemical desorption is the dominant dominant route for the supply of these gas-phase molecules. Because of chemical desorption, the abundances of H₂S ice and PH₃ ice are reduced compared with those in the model with $P_{\text{cd}} = 0\%$, and the dominant reservoirs of elemental S and P are the atomic forms.

The gas-phase H₂S abundance in the model with $P_{\text{cd}}(\text{H}_2\text{S}) = 3\%$ is $(1 - 4) \times 10^{-9}$ after 10^5 years. The predicted value is similar to that observed in the molecular cloud TMC1-CP $((0.6 - 6) \times 10^{-9}$, depending on the position in the cloud; Navarro-Almaida et al. 2020). The gas-phase PH₃ abundance in the model with $P_{\text{cd}}(\text{PH}_3) = 4\%$ is $(3 - 20) \times 10^{-11}$ after 10^5 years. To the best of our knowledge, PH₃ has not been detected in cold molecular clouds. Future high-sensitivity observations of the PH₃ $1_0 - 0_0$ transition at 266.9445136 GHz (Müller et al. 2001, 2005) toward cold molecular clouds such as TMC-1 would provide an interesting test of the surface chemistry of P.

The model with $P_{\text{cd}} = 1\%$, which is often assumed in astrochemical models, predicts gas-phase abundances of H₂S and PH₃ similar to those in the model with $P_{\text{cd}}(\text{H}_2\text{S}) = 3\%$ and $P_{\text{cd}}(\text{PH}_3) = 4\%$; the difference in the abundances is less than a factor of two. This weak dependence indicates that the loops of H₂S–HS and PH₃–PH₂ interconversions on dust grains are highly efficient and that the rate-limiting step of the desorption of H₂S and PH₃ in our models is the adsorption of atomic H. Notably, however, our rate-equation model, in

which a single type of adsorption site is considered, may overestimate the rate of the loops of H₂S–HS and PH₃–PH₂ interconversions. In reality, deep-potential sites can trap atomic H, slowing the loops of H₂S–HS and PH₃–PH₂ interconversions, as observed in our kMC models. To accurately evaluate the effect of chemical desorption under the ISM conditions, the binding energy distribution for atomic H should be considered by solving a gas and ice chemical network.

5. SUMMARY

Chemical desorption is caused by the energy released by reactions; after an exothermic surface reaction, some of the excess energy is dissipated into product’s translational energy in the direction perpendicular to the surface, leading to desorption (e.g., Fredon et al. 2017). Chemical desorption is usually included in modern gas–ice astrochemical models after Garrod et al. (2007); however, its efficiency is poorly constrained, especially desorption from water ice. Oba et al. (2019) experimentally studied chemical desorption upon the reaction of H₂S with H atoms on porous ASW. Nguyen et al. (2021) conducted similar laboratory studies for the reactions of PH₃ with H atoms. These studies demonstrated that H₂S and PH₃ can be lost from water ice surfaces by chemical desorption. They also estimated a chemical desorption probability for H₂S and PH₃ *per reactive species* (i.e., per incident H atom) of $\sim 1\%$ on porous ASW. As noted by Oba et al. (2018), the desorption probability per incident H atom corresponds to the lower limit of the desorption probability *per reactive event*, which astrochemical models require as inputs, because a substantial fraction of adsorbed H atoms on ASW surfaces would be thermally desorbed and subsequently consumed by the H₂ formation reaction on the surface. In the present work, we constrained the desorption probability of H₂S and PH₃ per reactive event on porous ASW by numerically simulating the laboratory experiments of Oba et al. (2019) and Nguyen et al. (2021). We used kinetic Monte Carlo simulations in which the position and movement of each chemical species on surfaces were tracked over time and in which the binding energy distributions of atomic H and H₂ were considered. Our findings are summarized as follows.

1. The chemical desorption probability of H₂S and PH₃ per hydrogenation event of the precursor species on porous ASW are constrained to $3 \pm 1.5\%$ and $4 \pm 2\%$, respectively.
2. These probabilities are consistent with a theoretical model of chemical desorption proposed by Fredon et al. (2021), with $\chi \sim 0.07\%$ (where χ is

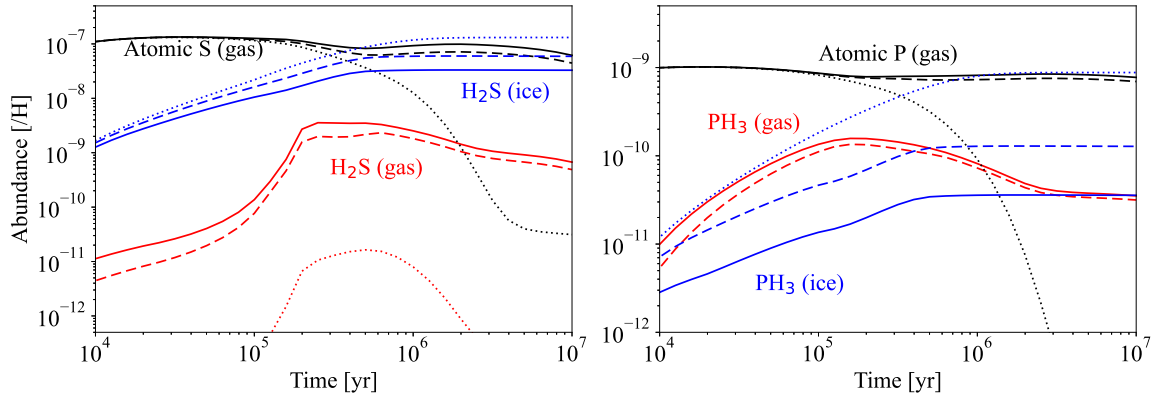


Figure 12. Temporal evolution of the abundances of S-bearing species (left panel) and P-bearing species (right panel) with respect to H nuclei. Solid lines represent models with $P_{\text{cd}}(\text{H}_2\text{S}) = 3\%$ and $P_{\text{cd}}(\text{PH}_3) = 4\%$, dashed lines represent models with $P_{\text{cd}}(\text{H}_2\text{S}) = P_{\text{cd}}(\text{PH}_3) = 1\%$, and dotted lines represent models with $P_{\text{cd}}(\text{H}_2\text{S}) = P_{\text{cd}}(\text{PH}_3) = 0\%$ (i.e., without chemical desorption of H_2S and PH_3).

a free parameter) describing the fraction of reaction energy transferred to the translational excitation of reaction products. Whether the Fredon et al. model with $\chi \sim 0.07$ provides reasonable estimates of P_{cd} for other reaction systems is unclear. Experimental and numerical studies of additional systems are required for better understanding of the chemical desorption process.

- As a byproduct, we constrained the binding energy distribution of atomic H. The abundance of H_2S became $\sim 40\%$ and $\sim 70\%$ of the initial H_2S abundance in the 20 K and 30 K experiments by Oba et al. (2019), respectively. These results indicate that $\sim 70\%$ of the adsorption sites on porous ASW should have $E_{\text{b}}(\text{H}) \lesssim 300$ K, whereas $\sim 40\%$ of adsorption sites should have $E_{\text{b}}(\text{H}) \lesssim 200$ K (see Section 3.1.1).

Finally, we stress that, for the chemical reactions systems on which the present work is focused, basic chemical data are available in the literature (e.g., rate coefficients and binding energies). Without these basic data

provided by computational chemistry and experiments, we could not have constrained the chemical desorption probability. Basic chemical data are critical not only for astrochemical models of astrophysical objects but also for extracting chemical parameters from laboratory experiments of surface reactions.

ACKNOWLEDGMENTS

KF acknowledges Naoko Yokomura and Yuri Aikawa for their assistance in developing the kMC code used in this work. YO acknowledges Naoki Watanabe, Akira Kouchi, Hiroshi Hidaka, and Nguyen Thanh for discussions of the experimental chemical desorption results. We are grateful to the anonymous referees for providing valuable comments that helped improve the manuscript. This work is partly supported by JSPS KAKENHI Grant numbers 17H06087, 20H05847, 21H01145, 21H04501, and 21K13967. Numerical computations were carried out in part on a PC cluster at the Center for Computational Astrophysics, National Astronomical Observatory of Japan.

APPENDIX

A. ADDITIONAL MODEL RESULTS

Figure 13 shows the results from additional models of the $\text{H}_2\text{S} + \text{H}$ system, where $E_{\text{b}}^{\text{min}}(\text{H}_2)$ is fixed at 150 K and f and $P_{\text{cd}}(\text{H}_2\text{S})$ are varied between 0.6 and 0.8 and between 5% and 20%, respectively. Among the nine different models shown in the figure, only three models can reasonably well reproduce the 30 K experiments (shown by thick lines in the figure): the model with $f = 0.7$ and $P_{\text{cd}}(\text{H}_2\text{S}) = 20\%$, the model with $f = 0.8$ and $P_{\text{cd}}(\text{H}_2\text{S}) = 5\%$, and the model with $f = 0.8$ and $P_{\text{cd}}(\text{H}_2\text{S}) = 10\%$. The first and third models overestimate the amounts of H_2S and HS desorbed from the surface at 10 K and 20 K compared with the amounts measured in the corresponding experiments. The second model moderately well reproduces the experiments at 10 K, 20 K, and 30 K simultaneously; however, the model tends to overestimate the amount of H_2S and HS desorbed from the surface compared with the experiments at 10 K and

20 K. Notably, this model is similar to our best-fit model ($f = 0.8$ vs 0.85 and $P_{\text{cd}}(\text{H}_2\text{S}) = 5\%$ vs. 3%); however, the reduced χ^2 for this model is greater than that for the best-fit model (2.38 vs 1.85).

B. POLYNOMIAL DISTRIBUTION VS. GAUSSIAN DISTRIBUTION

In our models, we assumed that the binding energy distributions for H₂ are described by a polynomial function (Eq. 9) from 780 K to $E_{\text{b}}^{\text{min}}$ on the basis of the experiments by [Amiaud et al. \(2006, 2015\)](#). The distribution at E_{b} lower than ~ 350 K was not constrained well in the experiments. We simply extrapolated the polynomial function to lower E_{b} values. Here, we check the effect of this extrapolation on the modeling results. We tested some models in which the H₂ binding energy followed a Gaussian distribution with a mean value of 270 K and a full-width at half-maximum (FWHM) of 190 K. The lower boundary of $E_{\text{b}}(\text{H}_2)$ was assumed to be 150 K, which roughly corresponds to the intermolecular potential energy of a H₂-H₂O dimer (~ 120 K; [Zhang et al. 1991](#)). As shown in Figure 14, this Gaussian distribution matches the polynomial distribution for $E_{\text{b}} \gtrsim 350$ K; by contrast, for lower E_{b} , the two distributions deviate.

Figure 15 shows the results of a small grid of models, where f and $P_{\text{cd}}(\text{H}_2\text{S})$ are varied between 0.6 and 0.8, and between 3% and 10%, respectively. As shown, no model can reproduce the experiments at 10 K, 20 K, and 30 K simultaneously. We conclude that there is no clear advantage to using the Gaussian distribution instead of the polynomial distribution.

REFERENCES

- Aikawa, Y., & Herbst, E. 1999, *ApJ*, 526, 314, doi: [10.1086/307973](https://doi.org/10.1086/307973)
- Amiaud, L., Fillion, J. H., Baouche, S., et al. 2006, *JChPh*, 124, 094702, doi: [10.1063/1.2168446](https://doi.org/10.1063/1.2168446)
- Amiaud, L., Fillion, J.-H., Dulieu, F., Momeni, A., & Lemaire, J.-L. 2015, *Physical Chemistry Chemical Physics (Incorporating Faraday Transactions)*, 17, 30148, doi: [10.1039/C5CP03985A](https://doi.org/10.1039/C5CP03985A)
- Aota, T., & Aikawa, Y. 2012, *ApJ*, 761, 74, doi: [10.1088/0004-637X/761/1/74](https://doi.org/10.1088/0004-637X/761/1/74)
- Asgeirsson, V., Jonsson, H., & Wikfeldt, K. T. 2017, *The Journal of Physical Chemistry C*, 121, 1648, doi: [10.1021/acs.jpcc.6b10636](https://doi.org/10.1021/acs.jpcc.6b10636)
- Bergner, J. B., Öberg, K. I., Walker, S., et al. 2019, *ApJL*, 884, L36, doi: [10.3847/2041-8213/ab48f9](https://doi.org/10.3847/2041-8213/ab48f9)
- Bertin, M., Romanzin, C., Doronin, M., et al. 2016, *ApJL*, 817, L12, doi: [10.3847/2041-8205/817/2/L12](https://doi.org/10.3847/2041-8205/817/2/L12)
- Blake, G. A., van Dishoeck, E. F., Jansen, D. J., Groesbeck, T. D., & Mundy, L. G. 1994, *ApJ*, 428, 680, doi: [10.1086/174278](https://doi.org/10.1086/174278)
- Cazaux, S., Carrascosa, H., Munoz Caro, G. M., et al. 2021, arXiv e-prints, arXiv:2110.04230. <https://arxiv.org/abs/2110.04230>
- Cazaux, S., Martín-Doménech, R., Chen, Y. J., Muñoz Caro, G. M., & González Díaz, C. 2017, *ApJ*, 849, 80, doi: [10.3847/1538-4357/aa8b0c](https://doi.org/10.3847/1538-4357/aa8b0c)
- Chang, Q., Cuppen, H. M., & Herbst, E. 2007, *A&A*, 469, 973, doi: [10.1051/0004-6361:20077423](https://doi.org/10.1051/0004-6361:20077423)
- Chang, Q., & Herbst, E. 2012, *ApJ*, 759, 147, doi: [10.1088/0004-637X/759/2/147](https://doi.org/10.1088/0004-637X/759/2/147)
- Chantzios, J., Rivilla, V. M., Vasyunin, A., et al. 2020, *A&A*, 633, A54, doi: [10.1051/0004-6361/201936531](https://doi.org/10.1051/0004-6361/201936531)
- Charnley, S. B., & Millar, T. J. 1994, *MNRAS*, 270, 570, doi: [10.1093/mnras/270.3.570](https://doi.org/10.1093/mnras/270.3.570)
- Chuang, K. J., Fedoseev, G., Qasim, D., et al. 2018, *ApJ*, 853, 102, doi: [10.3847/1538-4357/aaa24e](https://doi.org/10.3847/1538-4357/aaa24e)
- Collings, M. P., Anderson, M. A., Chen, R., et al. 2004, *MNRAS*, 354, 1133, doi: [10.1111/j.1365-2966.2004.08272.x](https://doi.org/10.1111/j.1365-2966.2004.08272.x)
- Cuppen, H. M., & Herbst, E. 2007, *ApJ*, 668, 294, doi: [10.1086/521014](https://doi.org/10.1086/521014)
- Cuppen, H. M., Karssemeijer, L. J., & Lamberts, T. 2013, *Chemical Reviews*, 113, 8840, doi: [10.1021/cr400234a](https://doi.org/10.1021/cr400234a)
- Dartois, E., Augé, B., Boduch, P., et al. 2015, *A&A*, 576, A125, doi: [10.1051/0004-6361/201425415](https://doi.org/10.1051/0004-6361/201425415)
- Dulieu, F., Congiu, E., Noble, J., et al. 2013, *Scientific Reports*, 3, 1338, doi: [10.1038/srep01338](https://doi.org/10.1038/srep01338)
- Dupuy, J. L., Lewis, S. P., & Stancil, P. C. 2016, *The Astrophysical Journal*, 831, 54, doi: [10.3847/0004-637x/831/1/54](https://doi.org/10.3847/0004-637x/831/1/54)
- Fredon, A., Lamberts, T., & Cuppen, H. M. 2017, *ApJ*, 849, 125, doi: [10.3847/1538-4357/aa8c05](https://doi.org/10.3847/1538-4357/aa8c05)
- Fredon, A., Radchenko, A. K., & Cuppen, H. M. 2021, *Accounts of Chemical Research*, 54, 745, doi: [10.1021/acs.accounts.0c00636](https://doi.org/10.1021/acs.accounts.0c00636)
- Fuente, A., Goicoechea, J. R., Pety, J., et al. 2017, *ApJL*, 851, L49, doi: [10.3847/2041-8213/aaa01b](https://doi.org/10.3847/2041-8213/aaa01b)
- Furuya, K., Aikawa, Y., Hincelin, U., et al. 2015, *A&A*, 584, A124, doi: [10.1051/0004-6361/201527050](https://doi.org/10.1051/0004-6361/201527050)
- Furuya, K., & Persson, M. V. 2018, *MNRAS*, 476, 4994, doi: [10.1093/mnras/sty553](https://doi.org/10.1093/mnras/sty553)

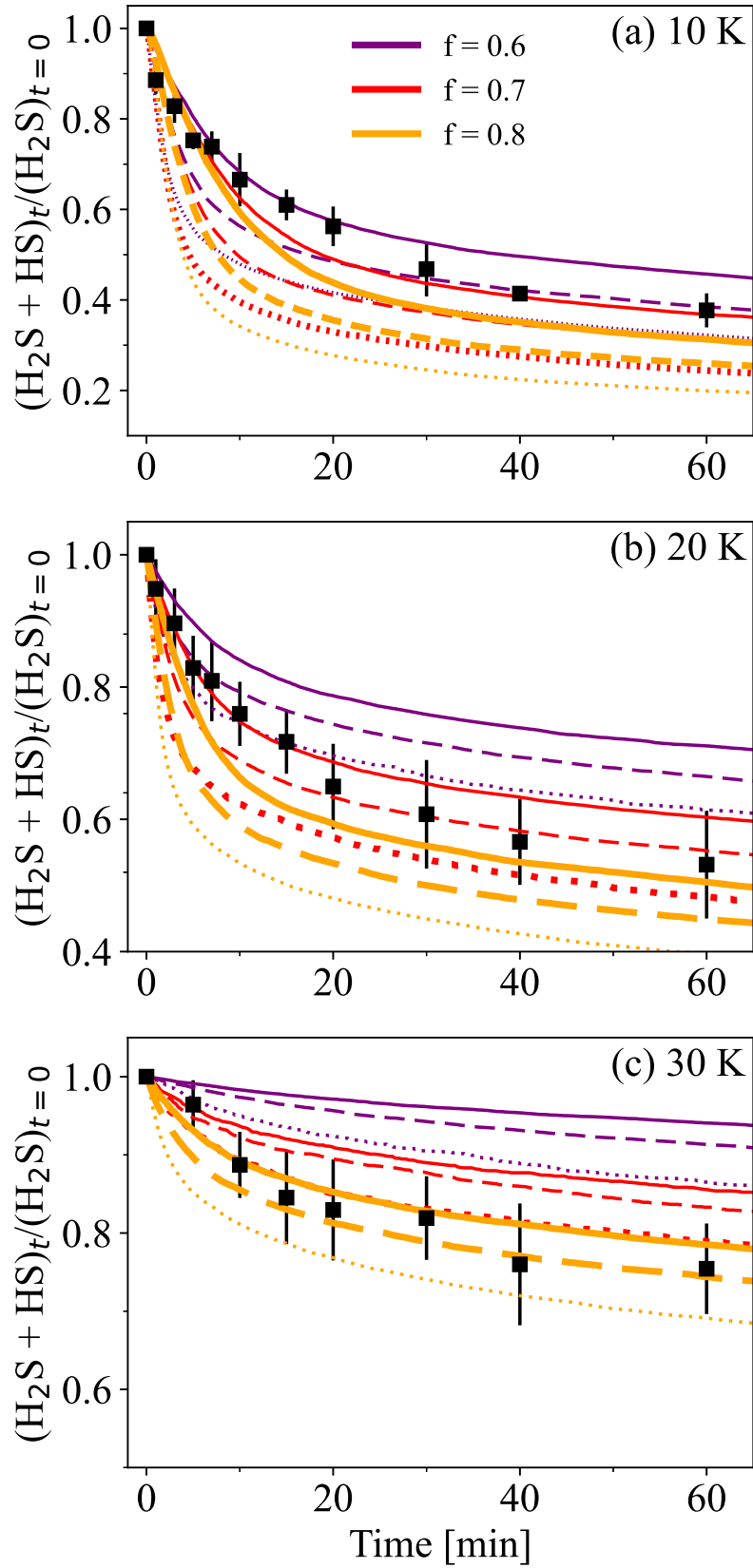


Figure 13. Total sulfur ($\text{H}_2\text{S} + \text{HS}$) abundance with respect to the initial H_2S abundance on porous ASW at 10 K (panel a), 20 K (panel b), and 30 K (panel c) as functions of H-atom exposure time in the kMC simulations (lines) and in the experiments by Oba et al. (2019) (black squares). Solid, dashed, and dotted lines represent the models with $P_{c1}(\text{H}_2\text{S})$ values of 5%, 10%, and 20%, respectively. The models with different f values are represented in different colors. In all the models, $E_b^{\text{min}}(\text{H}_2)$ is set to 150 K.

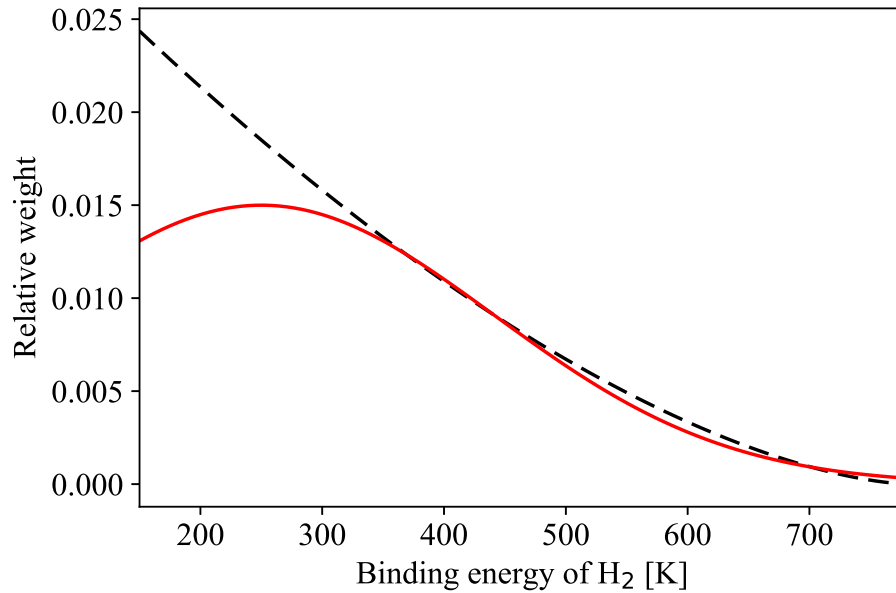


Figure 14. Binding energy distribution for H₂ assuming a Gaussian distribution (red) and a polynomial function (black). See the text for additional details.

- Garrod, R. T. 2008, *A&A*, 491, 239, doi: [10.1051/0004-6361:200810518](https://doi.org/10.1051/0004-6361:200810518)
- . 2013, *ApJ*, 765, 60, doi: [10.1088/0004-637X/765/1/60](https://doi.org/10.1088/0004-637X/765/1/60)
- Garrod, R. T., & Herbst, E. 2006, *A&A*, 457, 927, doi: [10.1051/0004-6361:20065560](https://doi.org/10.1051/0004-6361:20065560)
- Garrod, R. T., Wakelam, V., & Herbst, E. 2007, *A&A*, 467, 1103, doi: [10.1051/0004-6361:20066704](https://doi.org/10.1051/0004-6361:20066704)
- Geppert, W. D., Hamberg, M., Thomas, R. D., et al. 2006, *Faraday Discussions*, 133, 177, doi: [10.1039/B516010C](https://doi.org/10.1039/B516010C)
- Gibson, M. A., & Bruck, J. 2000, *Journal of Physical Chemistry A*, 104, 1876, doi: [10.1021/jp993732q](https://doi.org/10.1021/jp993732q)
- Gillespie, D. T. 1976, *Journal of Computational Physics*, 22, 403, doi: [https://doi.org/10.1016/0021-9991\(76\)90041-3](https://doi.org/10.1016/0021-9991(76)90041-3)
- Graedel, T. E., Langer, W. D., & Frerking, M. A. 1982, *ApJS*, 48, 321, doi: [10.1086/190780](https://doi.org/10.1086/190780)
- Hama, T., Kuwahata, K., Watanabe, N., et al. 2012, *ApJ*, 757, 185, doi: [10.1088/0004-637X/757/2/185](https://doi.org/10.1088/0004-637X/757/2/185)
- Hama, T., Ueta, H., Kouchi, A., & Watanabe, N. 2015, *Proceedings of the National Academy of Science*, 112, 7438, doi: [10.1073/pnas.1501328112](https://doi.org/10.1073/pnas.1501328112)
- Hama, T., Yabushita, A., Yokoyama, M., Kawasaki, M., & Andersson, S. 2009, *JChPh*, 131, 054508, doi: [10.1063/1.3191731](https://doi.org/10.1063/1.3191731)
- Hasegawa, T. I., & Herbst, E. 1993, *MNRAS*, 263, 589, doi: [10.1093/mnras/263.3.589](https://doi.org/10.1093/mnras/263.3.589)
- He, J., Emtiaz, S. M., & Vidali, G. 2017, *ApJ*, 851, 104, doi: [10.3847/1538-4357/aa9a3e](https://doi.org/10.3847/1538-4357/aa9a3e)
- Hidaka, H., Miyauchi, N., Kouchi, A., & Watanabe, N. 2008, *Chemical Physics Letters*, 456, 36, doi: [10.1016/j.cplett.2008.03.010](https://doi.org/10.1016/j.cplett.2008.03.010)
- Ivlev, A. V., Röcker, T. B., Vasyunin, A., & Caselli, P. 2015, *ApJ*, 805, 59, doi: [10.1088/0004-637X/805/1/59](https://doi.org/10.1088/0004-637X/805/1/59)
- Jenkins, E. B. 2009, *ApJ*, 700, 1299, doi: [10.1088/0004-637X/700/2/1299](https://doi.org/10.1088/0004-637X/700/2/1299)
- Jiménez-Escobar, A., & Muñoz Caro, G. M. 2011, *A&A*, 536, A91, doi: [10.1051/0004-6361/201014821](https://doi.org/10.1051/0004-6361/201014821)
- Karssemeijer, L. J., Ioppolo, S., van Hemert, M. C., et al. 2014, *ApJ*, 781, 16, doi: [10.1088/0004-637X/781/1/16](https://doi.org/10.1088/0004-637X/781/1/16)
- Kimmel, G. A., Stevenson, K. P., Dohnálek, Z., Smith, R. S., & Kay, B. D. 2001, *The Journal of Chemical Physics*, 114, 5284, doi: [10.1063/1.1350580](https://doi.org/10.1063/1.1350580)
- Kuwahata, K., Hama, T., Kouchi, A., & Watanabe, N. 2015, *PhRvL*, 115, 133201, doi: [10.1103/PhysRevLett.115.133201](https://doi.org/10.1103/PhysRevLett.115.133201)
- Lamberts, T., Cuppen, H. M., Fedoseev, G., et al. 2014, *A&A*, 570, A57, doi: [10.1051/0004-6361/201424252](https://doi.org/10.1051/0004-6361/201424252)
- Lamberts, T., & Kästner, J. 2017, *Journal of Physical Chemistry A*, 121, 9736, doi: [10.1021/acs.jpca.7b10296](https://doi.org/10.1021/acs.jpca.7b10296)
- Lefloch, B., Vastel, C., Viti, S., et al. 2016, *MNRAS*, 462, 3937, doi: [10.1093/mnras/stw1918](https://doi.org/10.1093/mnras/stw1918)
- Maté, B., Cazaux, S., Satorre, M. Á., et al. 2020, *A&A*, 643, A163, doi: [10.1051/0004-6361/202038705](https://doi.org/10.1051/0004-6361/202038705)
- McGuire, B. A. 2018, *ApJS*, 239, 17, doi: [10.3847/1538-4365/aae5d2](https://doi.org/10.3847/1538-4365/aae5d2)
- Minh, Y. C., Irvine, W. M., & Ziurys, L. M. 1989, *ApJL*, 345, L63, doi: [10.1086/185553](https://doi.org/10.1086/185553)
- Minissale, M., & Dulieu, F. 2014, *The Journal of Chemical Physics*, 141, 014304, doi: [10.1063/1.4885847](https://doi.org/10.1063/1.4885847)
- Minissale, M., Dulieu, F., Cazaux, S., & Hocuk, S. 2016, *A&A*, 585, A24, doi: [10.1051/0004-6361/201525981](https://doi.org/10.1051/0004-6361/201525981)

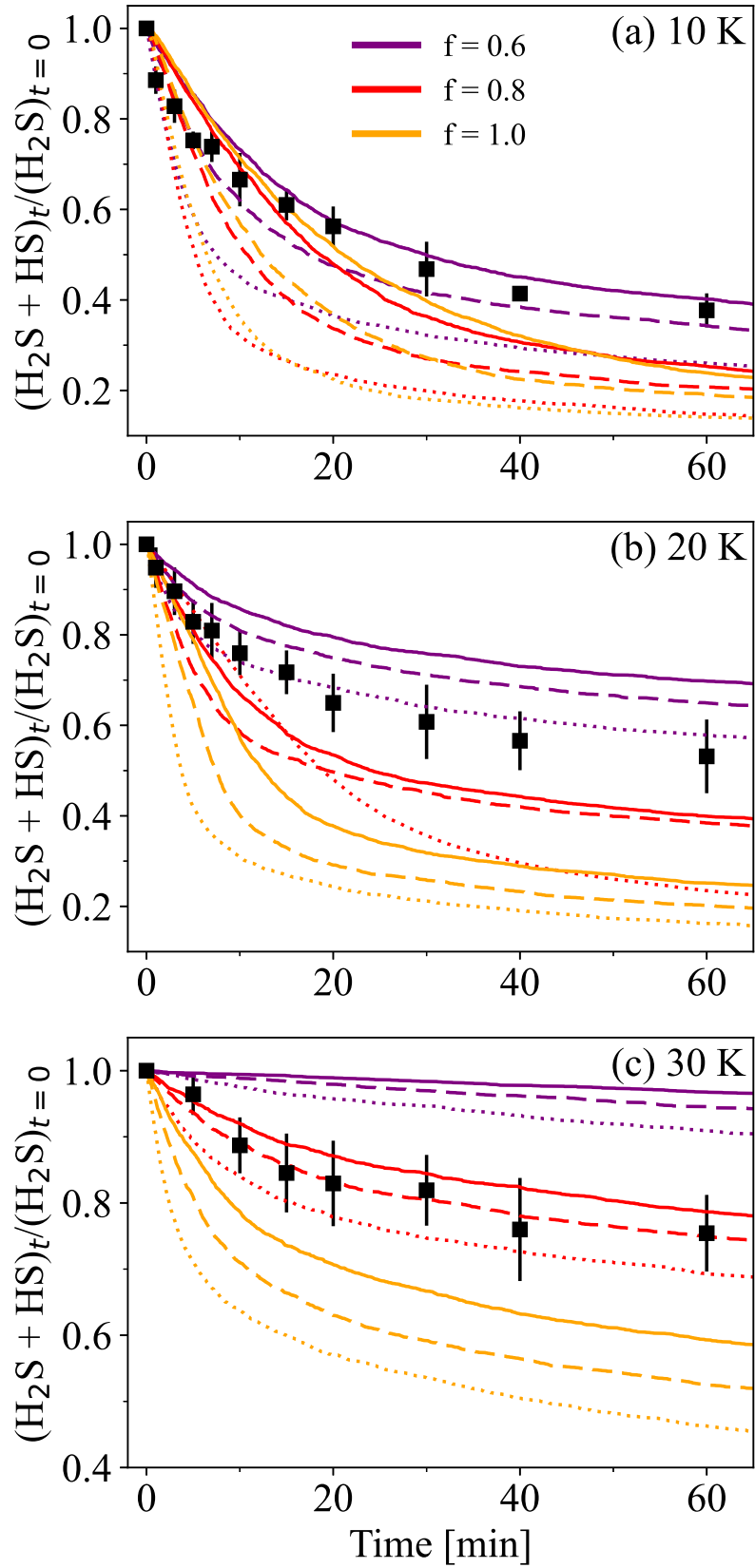


Figure 15. Total sulfur ($\text{H}_2\text{S} + \text{HS}$) abundance with respect to the initial H_2S abundance on porous ASW at 10 K (panel a), 20 K (panel b), and 30 K (panel c) as functions of H-atom exposure time in the models, where the binding energies for atomic H and H_2 follow a Gaussian distribution (lines). Black squares represent the experiments by Oba et al. (2019). Solid, dashed, and dotted lines represent the models with $P_{\text{cd}}(\text{H}_2\text{S})$ of 3%, 5%, and 10%, respectively. The models with different f are represented in different colors.

- Molpeceres, G., & Kästner, J. 2020, *Physical Chemistry Chemical Physics (Incorporating Faraday Transactions)*, 22, 7552, doi: [10.1039/D0CP00250J](https://doi.org/10.1039/D0CP00250J)
- . 2021, *ApJ*, 910, 55, doi: [10.3847/1538-4357/abe38c](https://doi.org/10.3847/1538-4357/abe38c)
- Müller, H. S. P., Schlöder, F., Stutzki, J., & Winnewisser, G. 2005, *Journal of Molecular Structure*, 742, 215, doi: [10.1016/j.molstruc.2005.01.027](https://doi.org/10.1016/j.molstruc.2005.01.027)
- Müller, H. S. P., Thorwirth, S., Roth, D. A., & Winnewisser, G. 2001, *A&A*, 370, L49, doi: [10.1051/0004-6361:20010367](https://doi.org/10.1051/0004-6361:20010367)
- Navarro-Almaida, D., Le Gal, R., Fuente, A., et al. 2020, *A&A*, 637, A39, doi: [10.1051/0004-6361/201937180](https://doi.org/10.1051/0004-6361/201937180)
- Nguyen, T., Oba, Y., Sameera, W. M. C., Kouchi, A., & Watanabe, N. 2021, *ApJ*, 918, 73, doi: [10.3847/1538-4357/ac0cf4](https://doi.org/10.3847/1538-4357/ac0cf4)
- Nguyen, T., Oba, Y., Shimonishi, T., Kouchi, A., & Watanabe, N. 2020, *ApJL*, 898, L52, doi: [10.3847/2041-8213/aba695](https://doi.org/10.3847/2041-8213/aba695)
- Oba, Y., Tomaru, T., Kouchi, A., & Watanabe, N. 2019, *ApJ*, 874, 124, doi: [10.3847/1538-4357/ab0961](https://doi.org/10.3847/1538-4357/ab0961)
- Oba, Y., Tomaru, T., Lamberts, T., Kouchi, A., & Watanabe, N. 2018, *Nature Astronomy*, 2, 228, doi: [10.1038/s41550-018-0380-9](https://doi.org/10.1038/s41550-018-0380-9)
- Ohishi, M., Irvine, W. M., & Kaifu, N. 1992, in *Astrochemistry of Cosmic Phenomena*, ed. P. D. Singh, Vol. 150, 171
- Pantaleone, S., Enrique-Romero, J., Ceccarelli, C., et al. 2021, arXiv e-prints, arXiv:2105.06843. <https://arxiv.org/abs/2105.06843>
- . 2020, *ApJ*, 897, 56, doi: [10.3847/1538-4357/ab8a4b](https://doi.org/10.3847/1538-4357/ab8a4b)
- Phuong, N. T., Chapillon, E., Majumdar, L., et al. 2018, *A&A*, 616, L5, doi: [10.1051/0004-6361/201833766](https://doi.org/10.1051/0004-6361/201833766)
- Rivière-Marichalar, P., Fuente, A., Le Gal, R., et al. 2021, arXiv e-prints, arXiv:2106.02430. <https://arxiv.org/abs/2106.02430>
- Sil, M., Srivastav, S., Bhat, B., et al. 2021, arXiv e-prints, arXiv:2105.14569. <https://arxiv.org/abs/2105.14569>
- Smith, R. G. 1991, *MNRAS*, 249, 172, doi: [10.1093/mnras/249.1.172](https://doi.org/10.1093/mnras/249.1.172)
- Smoluchowski, R. 1983, *The Journal of Physical Chemistry*, 87, 4229, doi: [10.1021/j100244a050](https://doi.org/10.1021/j100244a050)
- Taquet, V., Charnley, S. B., & Sipilä, O. 2014, *ApJ*, 791, 1, doi: [10.1088/0004-637X/791/1/1](https://doi.org/10.1088/0004-637X/791/1/1)
- Thorne, L. R., Anicich, V. G., Prasad, S. S., & Huntress, W. T., J. 1984, *ApJ*, 280, 139, doi: [10.1086/161977](https://doi.org/10.1086/161977)
- Turner, B. E., Tsuji, T., Bally, J., Guelin, M., & Cernicharo, J. 1990, *ApJ*, 365, 569, doi: [10.1086/169511](https://doi.org/10.1086/169511)
- Wakelam, V., Castets, A., Ceccarelli, C., et al. 2004, *A&A*, 413, 609, doi: [10.1051/0004-6361:20031572](https://doi.org/10.1051/0004-6361:20031572)
- Wakelam, V., & Herbst, E. 2008, *ApJ*, 680, 371, doi: [10.1086/587734](https://doi.org/10.1086/587734)
- Wakelam, V., Loison, J. C., Mereau, R., & Ruaud, M. 2017, *Molecular Astrophysics*, 6, 22, doi: [10.1016/j.molap.2017.01.002](https://doi.org/10.1016/j.molap.2017.01.002)
- Yamamoto, S. 2017, *Introduction to Astrochemistry: Chemical Evolution from Interstellar Clouds to Star and Planet Formation*, doi: [10.1007/978-4-431-54171-4](https://doi.org/10.1007/978-4-431-54171-4)
- Zhang, Q., Sabelli, N., & Buch, V. 1991, *JChPh*, 95, 1080, doi: [10.1063/1.461136](https://doi.org/10.1063/1.461136)